Surface Urban Energy and Water Balance Scheme (v2020a) in vegetated areas: parameter derivation and performance evaluation using FLUXNET2015 dataset

Hamidreza Omidvar[1], Ting Sun[1,✉], Sue Grimmond[1,✉], Dave Bilesbach[2], Andrew Black[3], Jiquan Chen[4], Zexia Duan[5], Zhiqiu Gao[5,6], Hiroki Iwata[7], Joseph P. McFadden[8]

[1] Department of Meteorology, University of Reading, Reading, RG6 6ET, UK
[2] Biological Systems Engineering Department, University of Nebraska, Lincoln, NE, 68588, USA
[3] Faculty of Land and Food System, University of British Columbia, Vancouver, BC, V6T 1Z4, CA
[4] Center for Global Change and Earth Observation, Department of Geography, Michigan State University, East Lansing, MI, 48824, USA
[5] Collaborative Innovation Centre on Forecast and Evaluation of Meteorological Disasters, School of Atmospheric Physics, Nanjing University of Information Science and Technology, Nanjing, 210044, China
[6] State Key Laboratory of Atmospheric Boundary Layer Physics and Atmospheric Chemistry, Institute of Atmospheric Physics, Chinese Academy of Sciences, Beijing, 100029, China
[7] Department of Environmental Science, Faculty of Science, Shinshu University, Nagano 390-8621, Japan
[8] Department of Geography, University of California, Santa Barbara, CA, 93106 USA

✉ *Correspondence to*: *ting.sun@reading.ac.uk; c.s.grimmond@reading.ac.uk*

ORCID:

Hamidreza Omidvar: *https://orcid.org/0000-0001-8124-7264*
Ting Sun: *https://orcid.org/0000-0002-2486-6146*
Sue Grimmond: *https://orcid.org/0000-0002-3166-9415*
Dave Bilesbach: *https://orcid.org/0000-0001-8661-9178*
Andrew Black: *https://orcid.org/0000-0001-9292-1146*
Jiquan Chen: *https://orcid.org/0000-0003-0761-9458*
Zexia Duan: *https://orcid.org/0000-0003-2822-7066*
Zhiqiu Gao: *https://orcid.org/0000-0001-8256-005X*
Hiroki Iwata: *https://orcid.org/0000-0002-8962-8982*
Joseph P. McFadden: *https://orcid.org/0000-0002-5869-7774*

Abstract

To compare urban and rural areas, the fully vegetated areas (e.g. deciduous trees, evergreen trees and grass) commonly found adjacent to cities need to be modelled. Here we provide a general workflow to derive parameters for SUEWS (Surface Urban Energy and Water Balance Scheme), including those associated with vegetation phenology (via leaf area index, LAI), heat storage and surface conductance. As expected, attribution analysis of bias in SUEWS modelled Q_E finds the surface conductance (g_s) plays the dominant role, hence there is need for more estimates of surface conductance parameters. The workflow is applied at 38 FLUXNET sites. The derived parameters vary between sites with the same plant functional type (PFT), demonstrating the challenge of using a single set of parameters for a PFT. SUEWS skill at simulating monthly and hourly latent heat flux (Q_E) is examined using the site-specific derived parameters, with the default NOAH surface conductance parameters (Chen et al. 1996). Overall evaluation for two years has similar metrics for both configurations: median hit rate between 0.6 and 0.7, median mean absolute error less than 25 W m^{-2}, and median mean bias error ~5 W m^{-2}. Performance differences are more evident at monthly and hourly scales, with larger mean bias error (monthly: ~40 W m^{-2}; hourly ~30 W m^{-2}) results using the NOAH-surface conductance parameters, suggesting that they should be used with caution. Assessment of sites with contrasting Q_E performance demonstrates how critical capturing the LAI dynamics is to the SUEWS prediction skills of g_s and Q_E. Generally g_s is poorest in cooler periods (more pronounced at night, when underestimated by ~3 mm s^{-1}). Given the global LAI data availability and the workflow provided in this study, any site to be simulated should benefit.

Keywords: SUEWS, FLUXNET, NOAH, LAI, surface conductance, Penman-Monteith equation

1 Introduction

The Surface Urban Energy and Water Balance Scheme (SUEWS, Grimmond et al., 1986, 1991, Grimmond & Oke 1991, Järvi et al., 2011) is widely used to simulate urban surface energy and hydrological fluxes, with heat and water released by anthropogenic activities accounted for (Grimmond et al., 1986; Grimmond, 1992). SUEWS characterises the heterogeneity of urban surfaces allowing an integrated mix of seven land covers within a grid cell (neighbourhood scale: O(0.1–10 km)) of impervious (buildings, paved) and pervious (evergreen trees/shrubs, deciduous trees/shrubs, grass, soil, water) types. Although SUEWS has been evaluated in cities around the globe (e.g. Karsisto et al., 2016, Ward et al., 2016, Ao et al., 2018, Kokkonen et al., 2018, Harshan et al., 2018) with varying mixes of integrated

impervious-pervious land covers, its performance has not been comprehensively examined in fully vegetated areas that commonly occur adjacent to cities.

One common and demanding application of urban climate models, including SUEWS, is to examine the very well-known canopy layer urban heat island effects – parts of cities are often warmer than their surroundings at night – and to understand the causes (Oke 1973, 1982). This requires both the "rural" context – usually characterised by pervious land cover – to be simulated appropriately ideally using the same modelling framework. As SUEWS v2020a (Tang et al. 2021) can diagnose near surface meteorology in the roughness sub-layer and canopy layer (e.g., air temperature and humidity at 2 m agl (above ground level), wind speed at 10 m agl), it is essential to ensure that any urban-rural comparison in these diagnostics has the proper rural skill and parameters (i.e. coefficient values used in parameterisations).

For meso-scale numerical weather prediction (NWP) of an urban region, both rural and urban areas need to be simulated. With plans to couple SUEWS to a meso-scale model (e.g. Weather Research and Forecasting (WRF), Skamarock and Klemp (2008)), most regions have extensive areas that have completely pervious grid cells. As these need to be simulated using a consistent surface scheme, it is essential to have appropriate parameters for these areas.

Central to the SUEWS biophysics, is the Penman-Monteith approach (Penman 1948; Monteith 1965) with a Jarvis-type (Jarvis 1976) surface moisture conductance (Grimmond and Oke 1991). Despite various parameters having been derived to account for different urban areas (e.g. land cover differences) and regions (e.g. high/mid-latitude) to allow for changing phenology, conductance and storage heat flux related parameters (e.g. Järvi et al. 2011, 2014; Ward et al. 2016), urban parameter estimates are lacking partly because of limited observations and lack of a standard workflow for deriving parameters. Other land surface schemes have parameters for a wide range of plant functional types (PFT) (e.g. NOAH within WRF, Chen et al. 1996, Chen and Dudhia 2001) but are often derived from a small number of observational sites and their widespread applicability is unexamined. For example, NOAH largely adopted values from the HAPEX-MOBILHY observational program (Andre et al. 1986) following Noilhan and Planton (1989).

FLUXNET (Baldocchi et al., 2001), a global network of research sites that monitor surface-atmosphere exchanges of carbon, water, and energy using the eddy covariance technique, provide unprecedented possibilities to advance the process-based land surface modelling with a comprehensive collection of datasets for either development (e.g. Stöckli et al. 2008) or evaluation (e.g. Zhang et al. 2017). Extensive analysis of FLUXNET datasets for the variety of terrestrial PFTs have considered various surface

atmosphere controls (e.g., albedo: Cescatti et al. 2012; latent heat flux: Ershadi et al. 2014; spatiotemporal representativeness: Chu et al. 2017, Villarreal and Vargas 2021; energy balance closure: Franssen et al. 2010; landscape heterogeneity: Göckede et al. 2008, Stoy et al. 2013) to enhance understanding of land-atmosphere interactions. As such, this is an ideal data source for deriving widely applicable parameters and assessing performance of SUEWS over different land cover types.

In this work, we develop general workflows (Fig. 1) to derive vegetation related parameters associated with phenology, the storage heat flux and surface moisture conductance; and comprehensively examine model skill in modelling latent heat fluxes. We briefly review the key vegetation biophysics schemes in SUEWS (Sect. 2), describe the FLUXNET2015 (Pastorello et al. 2020) and auxiliary datasets used (Sect. 3), and outline the workflows for deriving parameters (Sect. 4). To assess the quality of the derived parameters the SUEWS modelled latent heat flux is evaluated (Sect. 5). Model parameters related to surface conductance are derived for NOAH at the PFT level (Appendix A) as well as those related to surface roughness based on FLUXNET2015 dataset at the site level (Appendix B). Other model parameters derived following workflows (Sect. 4) are also provided (Appendix C). The source code, input data and model simulations analysed are provided in Sun et al. (2021).

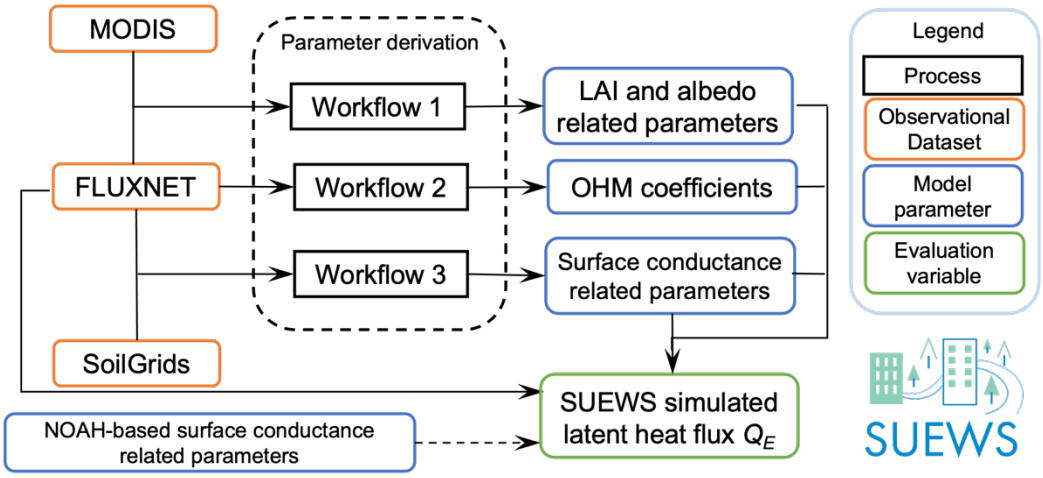

Figure 1 *Overview of workflows to derive parameters, to undertake and to evaluate simulations. Acronyms are defined in Sect. 2 and 3. More details are provided in Figures 3, 5, and 6.* ~~*At the bottom right is the SUEWS logo introduced since v2020a.*~~

2 SUEWS model

2.1 Overview of SUEWS physics for vegetated areas

Surface Urban Energy and Water Balance Scheme (SUEWS) is a local-scale land surface model for simulating the surface energy and hydrological fluxes (Grimmond and Oke 1986, 1991; Järvi et al. 2011,

2014; Offerle et al. 2003; Ward et al. 2016) without requiring specialised computing facilities. It has been extensively evaluated and applied in many cities (Lindberg et al.'s (2018) Table 3, Sun and Grimmond's (2019) Table 1). Other details of how SUEWS computes the surface energy, water and carbon fluxes are given in recent model description papers (Järvi et al., 2011; Ward et al., 2016; Järvi et al., 2019).

The surface energy and water balances are directly linked by the turbulent latent heat flux (Q_E) or its mass equivalent evaporation (E) (Grimmond and Oke 1986, 1991):

$$Q^* + Q_F = Q_H + Q_E + \Delta Q_S \quad (1)$$

$$P + I_e = E + R + \Delta S \quad (2)$$

where Q^* is the net all-wave radiation flux, Q_F is the anthropogenic heat flux, Q_H is the turbulent sensible heat flux, ΔQ_S the net storage heat flux, and P, I_e, ΔS and R are precipitation, external water use, net change in the water storage (e.g. canopy, soil moisture, water bodies) and runoff, respectively. The sites selected in this work are assumed to have no irrigation, so I_e is assumed to be 0 mm s^{-1}.

In SUEWS, a modified Penman-Monteith equation (Penman, 1948; Monteith, 1965) is used to compute Q_E with an expectation in cities that the anthropogenic heat flux (Q_F) is greater than zero (Grimmond and Oke, 1991):

$$Q_E = \frac{s(Q^* + Q_F - \Delta Q_S) + \frac{\rho c_p VPD}{r_a}}{s + \gamma\left(1 + \frac{r_s}{r_a}\right)} \quad (3)$$

However, with our current focus on extensive (non-urban) pervious areas Q_F is assumed to be 0 W m^{-2}. The atmospheric state is obtained from the slope of saturation water vapour pressure curve with respect to air temperature (s, units: Pa K^{-1}), density of air (ρ, kg m^{-3}), specific heat of air at constant pressure (c_p, J K^{-1} kg^{-1}), vapour pressure deficit (VPD, Pa), psychrometric 'constant' (γ,: Pa K^{-1}), and the aerodynamic resistance for water vapour (r_a, units: s m^{-1}).

Under given ambient meteorological conditions (e.g., incoming solar radiation $K_{\downarrow}$, air temperature T_a, humidity) at an extensive vegetated site, Q_E from this method is sensitive to the estimation of available energy (i.e. $Q^* - \Delta Q_S$), aerodynamic resistance r_a and surface resistance r_s. Hence, the critical vegetation related parameters (Table 1) are addressed with these caveats and/or assumptions:

- surface emissivity ε_0 and canopy water storage capacity S_i are assumed to the same as reported in Ward et al. (2016)
- aerodynamic resistance r_a is highly dependent on aerodynamic parameters that vary with canopy height (H_c) and leaf area index (LAI) (Kent et al., 2017; Appendix B). The temporal varying H_c is obtained from FLUXNET2015 (Sect. 2.2.3). LAI varies with phenology (Sect. 2.2.1)

Table 1 *Parameters and the first process they are used in by SUEWS (i.e. most impact multiple variables). Sources (S) include this study (*), Ward et al. (2016) (W16) and FLUXNET2015 (F15, Pastorello et al. 2020) where values are given (Table: T#, Sect.: S#) or used in individual equations (E). Two key phenology periods are related to growing and senescence degree days (GDD, SDD).*

Category	Symbol	Definition	Value			E	S
Leaf Area Index (LAI)	LAI_{min}	Minimum LAI	TC1			3	*
	LAI_{max}	Maximum LAI	TC1			3	*
	$T_{base,GDD}$	Base temperature for SDD	TC1			4	*
	$T_{base,SDD}$	Base temperature for GDD	TC1			4	*
	GDD_{full}	Ending GDD at LAI_{max}	TC1			5	*
	SDD_{full}	Ending SDD at LAI_{min}	TC1			5	*
	$\omega_{1(2),GDD\ (SDD)}$	Curve factors used in the LAI model dependent on GDD (SDD)	TC1			3	*
Radiation	$\alpha_{LAI_{\min}}$	Albedo at LAI_{min}	TC1			6	*
	$\alpha_{LAI_{\max}}$	Albedo at LAI_{max}	TC1			6	*
	ε_0	Emissivity	EveTr	DecTr	Grass		W16
			0.98	0.98	0.93		
Storage heat flux	a_1, a_2, a_3	Objective Hysteresis Model (OHM) coefficients	TC2			7	*
Aerodynamic resistance	H_c	Vegetation height	F15 varies				F15
	z_{0m}	Roughness length for momentum	S2.2.3/B			9/B1	*
	z_d	Zero plane displacement	S2.2.3/B			9/B1	*
Surface resistance	g_{max}	Maximum surface conductance	TC3			14	*
	G_K	Solar radiation related parameter	TC3			15	*
	$G_{q,base}$, $G_{q,shape}$	Specific humidity related parameters for base value and curve shape	TC3			16	*
	G_T	Air temperature related parameter	TC3			17	*
	T_H, T_L	Temperature limits for switching off evaporation	TC3			17	*
	G_θ	Soil moisture related parameter	TC3			18	*
	$\Delta\theta_{WP}$	Soil moisture deficit at wilting point	TC3			18	*
Water storage	S_i	Canopy water storage capacity (mm)	EveTr	DecTr	Grass	21	W16
			0.8	1.3	1.9		

2.2 Q_E related sub-schemes in SUEWS

2.2.1 Leaf Area Index (LAI) and Radiation

In SUEWS, leaf growth is tiggered by reaching a critical growing degree days (GDD) threshold ($T_{base,GDD,i}$), and similarly for leaf fall by senescence degree days ($SDD, T_{base,SDD,i}$) using daily (d) mean air temperatures (T_d) based on the previous day (d - 1) for each vegetation type i (one of evergreen trees, deciduous trees and grass). For forests and grass we use (Järvi et al., 2011):

$$LAI_{d,i} = \begin{cases} min(LAI_{max,i}, LAI_{d-1,i}^{\omega_{1,GDD,i}} GDD_{d,i}\ \omega_{2,GDD,i} + LAI_{d-1,i}), & T_{base,SDD,i} < T_{d-1} < T_{base,GDD,i} \\ max\left(LAI_{min,i}, LAI_{d-1,i}\ \omega_{1,SDD,i}(1 - SDD_{d,i})\ \omega_{2,SDD,i} + LAI_{d-1,i}\right), & T_{base,GDD,i} < T_{d-1} < T_{base,SDD,i} \end{cases} \quad (4)$$

with $\omega_{1/2,GDD/SDD,i}$ curve factors needing to be derived. T_{d-1} is derived from the daily maximum ($T_a^{\max}$) and minimum ($T_a^{\min}$) air temperature of the previous day:

$$T_{d-1} = \frac{T_a^{\max} + T_a^{\min}}{2} \tag{5}$$

For each site and vegetation type i, the maximum and minimum LAI values ($LAI_{max,i}$, $LAI_{min,i}$) and $T_{base,GDD}$ and $T_{base,SDD}$ are determined for each site (Sect. 4.1). For sites at higher latitude (e.g. > 60 °), other characteristics – such as day-length and photo period – are helpful to account for corresponding LAI controls (Bauerle et al., 2012; Gill et al., 2015).

LAI influences several processes in SUEWS – such as dynamics of surface conductance (later in Sect. 2.2.4) and albedo – the latter varies with daily LAI between a minimum ($\alpha_{LAI_{\min}}$) and maximum ($\alpha_{LAI_{\max}}$) by vegetation type:

$$\alpha_{d,i} = \alpha_{d-1,i} + \left(\alpha_{\mathrm{LAI,max},i} - \alpha_{\mathrm{LAI,min},i}\right)\frac{LAI_{d,i} - LAI_{d-1,i}}{LAI_{\mathrm{max},i} - LAI_{\mathrm{min},i}} \tag{6}$$

We note the SUEWS urban snow module (Järvi et al., 2014) is not used in this work, so focus on snow-free conditions. This may bias some modelled α and subsequent fluxes, but evaluating the snow module is a large task in its own right.

Within SUEWS the albedo is used with the observed incoming shortwave radiation and longwave radiation to obtain Q^*. In the current analyses, the observed incoming longwave ($L_\downarrow$) and modelled outgoing longwave radiation ($L_\uparrow = (1-\varepsilon_0)L_\downarrow + \varepsilon_0\sigma T_s^4$ where ε_0 is the surface emissivity, σ is the Stefan Boltzmann constant (W m^{-2} K^{-4}), and T_s is the surface temperature (K)) are used. Table 1 gives the emissivity values used.

2.2.2 Storage heat flux

Storage heat flux ΔQ_S is simulated with the objective hysteresis model (OHM (Grimmond et al., 1991)):

$$\Delta Q_S = \sum_i f_i \left[a_{1,i}Q^* + a_{2,i}\frac{\partial Q^*}{\partial t} + a_{3,i}\right] \tag{7}$$

where f_i is the plan area (or 3-dimensional fraction area, Grimmond et al. 1991, Grimmond and Oke 1999) fraction of surface i, $a_{1\text{-}3}$ the OHM coefficients (Sect. 4.2), and t time.

2.2.3 Aerodynamic resistance

Aerodynamic resistance r_a is obtained from (Järvi et al., 2011; van Ulden and Holtslag, 1985):

$$r_a = \frac{\left[\ln\left(\frac{z_m - z_d}{z_{0m}} - \psi_m(\zeta)\right)\right]\left[\ln\left(\frac{z_m - z_d}{z_{0v}} - \psi_v(\zeta)\right)\right]}{\kappa^2 u}, \tag{8}$$

where z_m is the measurement height for mean wind speed (u) and κ the von Kármán constant (0.4 assumed); the aerodynamic parameters z_d (zero plane displacement height) and z_{0m} (roughness length for the momentum) are estimated as a function of canopy height H_c (Garratt 1990; Grimmond and Oke, 1999):

$$z_{0m} = f_0 \, H_c \tag{9}$$

$$z_d = f_d \, H_c \tag{10}$$

with f_0 and f_d being vegetation-based coefficients (see Appendix B for derivation details). The stability parameter ζ $(= (z_m - z_d)/L)$ depends on the Obukhov length L. The atmospheric stability functions of momentum (ψ_m) and water vapour (ψ_v) for unstable condition are (Campbell and Norman, 1998):

$$\begin{aligned} \psi_v &= 2\ln\left[\frac{1+(1-16\zeta)^{1/2}}{2}\right], \\ \psi_m &= 0.6\psi_v \end{aligned} \tag{11}$$

and for stable condition (Campbell and Norman, 1998; Högström, 1988):

$$\begin{aligned} \psi_v &= -4.5\ln(1+\zeta) \\ \psi_m &= -6\ln(1+\zeta) \end{aligned} \tag{12}$$

2.2.4 Surface resistance (r_s) or conductance (g_s)

For completely wet surfaces, the surface resistance r_s is assumed to be 0 s m^{-1} (i.e. potential evaporation is calculated from Eq. 3). Otherwise r_s, or its inverse, surface conductance g_s, is parameterised with a Jarvis-type formulation (Jarvis 1976) in SUEWS (Grimmond and Oke 1991; Järvi et al. 2011; Ward et al. 2016):

$$r_s^{-1} = g_s = \sum_i \Big(g_{\max,i} \cdot f_i \cdot g(LAI_i)\Big)\, g(K_\downarrow) g(\Delta q) g(T_a) g(\Delta\theta_{soil})\,. \tag{13}$$

where g_s is determined from the i-th land cover areally weighted maximum surface conductance ($g_{\max,i}$) (with f_i =1 for a "homogeneous" site) and environmental (x) rescaling functions ($g(x)$) ranging between [0, 1], including:

- Leaf area index (LAI) (Ward et al. 2016):

$$g(LAI_i) = \frac{LAI_i}{LAI_{\max,i}} \tag{14}$$

is relative to the maximum LAI of land cover i ($LAI_{max,i}$). For bare soil surfaces (i.e. no vegetation), when LAI is irrelevant $g(LAI_i) = 1$.

- incoming shortwave radiation ($K_\downarrow$) (Stewart 1988):

$$g(K_\downarrow) = \frac{\dfrac{K_\downarrow}{G_K + K_\downarrow}}{\dfrac{K_{\downarrow,\max}}{G_K + K_{\downarrow,\max}}} \tag{15}$$

where the G_K parameter modifies the $K_\downarrow$ response, relative to $K_{\downarrow,\max}$ the maximum observed incoming shortwave radiation ($= 1200$ W m^{-2}): when $K_\downarrow$ approaches G_K, $g(K_\downarrow)$ reaches 50% of $g_{s,\max}\left(\frac{K_{\downarrow,\max}}{G_K+K_{\downarrow,\max}}\right)^{-1}$ (i.e., $g_{s,\max}$ normalised by $\frac{K_{\downarrow,\max}}{G_K+K_{\downarrow,\max}}$). At night $g(K_\downarrow)$ goes to 1.

- specific humidity deficit (Δq) (Ogink-Hendriks 1995):

$$g(\Delta q) = G_{q,base} + \left(1 - G_{q,base}\right)G_{q,shape}^{\Delta q} \tag{16}$$

where the specific humidity related parameters are for the 'base' $G_{q,base}$ and curve shape $G_{q,shape}$: the former indicates the limit of $g(\Delta q)$ when Δq approaches extremely large values, while the latter determines the curvature of the $g(\Delta q)$ (e.g., Fig. 9c)

- air temperature (T_a) (Stewart 1988):

$$g(T_a) = \frac{(T_a - T_L)(T_H - T_a)^{T_c}}{(G_T - T_L)(T_H - G_T)^{T_c}} \tag{17}$$

where $T_c = \frac{T_H - G_T}{G_T - T_L}$ is a function of the lower (T_L) and upper (T_H) limits when the evaporation occurs, and G_T the optimal temperature for evaporation to reach its potential maximum.

- soil moisture deficit ($\Delta\theta_{soil}$, difference between soil water capacity and soil moisture content) (Ward et al. 2016):

$$g(\Delta\theta_{soil}) = \frac{1-\exp\left(G_\theta(\Delta\theta_{soil} - \Delta\theta_{WP})\right)}{1-\exp(-G_\theta \Delta\theta_{WP})} \tag{18}$$

both the wilting point ($\Delta\theta_{\mathrm{WP}}$) and a soil type dependent parameter (G_θ) vary with soil and plant type. Appendix A gives the equivalent form used in the NOAH model for Eqn. 13.

SUEWS has a running water balance that accounts for the multiple surface types. The amount of water on the canopy of each surface (C_i) (Grimmond & Oke 1991) is used to vary the surface resistance between dry and wet ($r_s = 0$ s m^{-1}) by replacing r_s with r_{ss} (Shuttleworth, 1978):

$$r_{\mathrm{ss}} = \left[\frac{W}{r_b(s/\gamma + 1)} + \frac{(1 - W)}{r_s + r_b(s/\gamma + 1)}\right]^{-1} - r_b(s/\gamma + 1), \tag{19}$$

where W is a function of the relative amount of water present on each surface to its water storage capacity (S_i, Table 1):

$$W = \begin{cases} 1 & C_i \geq S_i \\ \dfrac{K - 1}{K - S_i/C_i} & C_i < S_i \end{cases}. \tag{20}$$

K depends on the aerodynamic and surface resistances:

$$K = \frac{(r_s/r_a)/(r_a - r_b)}{r_s + r_b(s/\gamma + 1)}, \tag{21}$$

where r_b, the boundary layer resistance, is a function of friction velocity u_* (Shuttleworth, 1983):

$$r_b = 1.1u_*^{-1} + 5.6u_*^{\frac{1}{3}}. \quad (22)$$

Eqn. 19-22 ensure that the surface resistance r_{ss} has a smooth transition from 0 (a completely wet surface) to r_s (a dry surface).

3 Global observational datasets used

We use three global datasets FLUXNET2015 (Pastorello et al. 2020), MODIS (Myneni et al., 2015) and SoilGrids (Hengl et al. 2014) to derive the parameters. The FLUXNET2015 surface energy fluxes and other meteorology observations are used for three purposes: to derive parameter values, force simulations and evaluate simulations. The remotely sensed (MODIS) derived LAI products are used for the LAI related parameters. To derive soil moisture related parameters the SoilGrids data are used. Unlike the FLUXNET2015 data, the latter two datasets are spatially continuous.

3.1 FLUXNET2015

The FLUXNET2015 dataset (Pastorello et al. 2020) is the newest version of the FLUXNET data products. The gap-filled dataset includes 212 flux sites from around the world. Although the FLUXNET focus is on local scale ecosystem CO_2 eddy covariance (EC) fluxes, it also includes water and energy EC fluxes plus other meteorological and biological data. The biosphere-atmosphere exchange dataset contains more than 1500 site-years for the period to the end of 2014. The open source package ONEFlux (Open Network-Enabled Flux processing pipeline; *https://github.com/fluxnet/ONEFlux*) is used to produce FLUXNET2015 (Pastorello et al. 2020).

Half-hourly observations (Table 2) are used from 38 sites (Table 3) in three regions (Fig. 2). These sites are selected to meet the following criteria (number of remaining sites that met the criteria):

1) sites with CC-BY 4.0 license (206/212).
2) data availability (56/206): require both MODIS LAI data (available from 2002, Sect. 3.2) and long-term continuity (defined here as ≥ 3 years for the multiple needs).
3) model capacity (38/56): the SUEWS v2020a LAI scheme used is driven by air temperature but other meteorological variables (e.g., rainfall) may strongly influence some sites phenology (Appendix D).

Unfortunately, no datasets are left after selection based on the above criteria for some regions (Fig. 2), including Africa, Asia and South America.

As SUEWS allows any grid cell to have three vegetation or plant functional types (PFT), with the sub-type or properties varying between grids, we subdivide the 38 sites into three classes using IGBP (Table 3) (code, number of sites):

a) Evergreen trees/shrubs (EveTr, 13): Evergreen Needleleaf Forests (ENF, 12), Evergreen Broadleaf Forests (EBF, 1)
b) Deciduous trees/shrubs (DecTr, 11): Mixed Forests (MF, 2), Deciduous Broadleaf Forests (DBF, 5), Open Shrublands (OSH, 1), Woody Savannas (WSA, 1), Savannas (SAV, 2).
c) Grass (14): Grasslands (GRA, 8), Croplands (CRO, 6).

The landscape heterogeneity of many FLUXNET EC flux measurements sites have been systematically examined by Stoy et al. (2013) using satellite imagery. Of the sites they examined, they found them to be located within homogeneous parts of the targeted PFT, but the larger landscape (~20 km) may have considerable variability. As a FLUXNET site is typically assigned to one PFT for land surface model development/evaluation (e.g. Stöckli et al. 2008, Zhang et al. 2017, Chu et al. 2021), we configure each as a homogeneous grid cell and assume f_i =1.

Table 2 *FLUXNET2015 (Pastorello et al. 2020) variables used in this work to derive parameters (P), to force (F) model simulations and to evaluate (E) models.*

Variable	Unit	Description	Usage
H_c	m (agl)	Canopy height	P
$K_\uparrow$	W m^{-2}	Outgoing solar radiation	P
$K_\downarrow$	W m^{-2}	Incoming solar radiation	P, F
$L_\uparrow$	W m^{-2}	Outgoing longwave radiation	P
$L_\downarrow$	W m^{-2}	Incoming longwave radiation	F
P	mm h^{-1}	Precipitation rate	P, F
PA	Pa	Station atmospheric pressure	P, F
Q^*	W m^{-2}	Net all-wave radiation	P
Q_E	W m^{-2}	Latent heat flux	P, E
Q_H	W m^{-2}	Sensible heat flux	P
RH	%	Relative humidity	P, F
T_a	℃	Air temperature	P, F
u	m s^{-1}	Wind speed	P, F
u_*	m s^{-1}	Friction velocity	P
VPD	Pa	Vapour pressure deficit	P
θ	m^3 m^{-3}	Volumetric soil water content	P

Table 3 *Key information about the FLUXNET2015 sites (Pastorello et al. 2020), and their DOI reference) used in this work: site name (country-name) with altitude above sea level (asl)) or anemometer sensor height above ground level (agl), More details about the simulation and analyses given in Sect. 5.1. The land cover type as defined based on IGBP (International Geosphere–Biosphere Programme) by the FLUXNET curators (https://fluxnet.org/data/badm-data-templates/igbp-classification/) with the crops (CRO) being: 1 - Rotation: cereal, potato, sugar beet (Moureaux et al., 2006), 2 - Rotation: winter barley, rapeseed, winter wheat, maize and spring barley at DE-Kli (Prescher et al., 2010), 3 - Continuous maize (https://doi.org/10.18140/FLX/1440084); 4 - Rotation: maize and soybean (https://doi.org/10.18140/FLX/1440085), 5- Rotation: maize and soybean (https://doi.org/10.18140/FLX/1440086). The SUEWS recommended vegetation/PFT class (informed by IGBP) data as used in this paper are given in Sun et al. (2021).*

Site	Latitude (°)	Longitude (°)	Altitude (m asl)	Measurement height z_m (m agl)	Parameter derivation period	Evaluation period	Temporal resolution (min)	No. of valid entries	IGBP	SUEWS	DOI
AT-Neu	47.1167	11.3175	970	3.0	2005 – 2012	2002 – 2004	30	33582	GRA	Grass	10.18140/FLX/1440121
AU-ASM	-22.283	133.249	607	11.7	2013 – 2014	2010 – 2012	30	33710	SAV	DecTr	10.18140/FLX/1440194
AU-DaS	-14.1593	131.388	73	21.0	2011 – 2014	2008 – 2010	30	34022	SAV	DecTr	10.18140/FLX/1440122
AU-Gin	-31.3764	115.714	51	15.0	2011 – 2011	2011 – 2013	30	28766	WSA	DecTr	10.18140/FLX/1440199
AU-Wom	-37.4222	144.094	705	30.0	2013 – 2014	2010 – 2012	30	34434	EBF	EveTr	10.18140/FLX/1440207
BE-Lon	50.5516	4.74623	167	2.7	2007 – 2014	2004 – 2006	30	34486	CRO[1]	Grass	10.18140/FLX/1440129
CA-Gro	48.2167	-82.1556	340	43.3	2006 – 2014	2003 – 2005	30	32669	MF	DecTr	10.18140/FLX/1440034
CA-Oas	53.6289	-106.198	530	39.0	1995 – 2010	2002 – 2004	30	34885	DBF	DecTr	10.18140/FLX/1440043
CA-Qfo	49.6925	-74.3421	382	24.0	2006 – 2010	2003 – 2005	30	32980	ENF	EveTr	10.18140/FLX/1440045
CA-SF2	54.2539	-105.878	520	9.1	2005 – 2005	2002 – 2004	30	31701	ENF	EveTr	10.18140/FLX/1440047
CA-SF3	54.0916	-106.005	540	20.0	2005 – 2007	2002 – 2004	30	34618	OSH	DecTr	10.18140/FLX/1440048
CA-TP4	42.7102	-80.3574	184	28.0	2005 – 2014	2002 – 2004	30	34533	ENF	EveTr	10.18140/FLX/1440053
CH-Cha	47.2102	8.41044	393	2.4	2006 – 2014	2005 – 2007	30	34480	GRA	Grass	10.18140/FLX/1440131
CH-Dav	46.8153	9.85591	1639	35.0	2005 – 2014	2002 – 2004	30	24456	ENF	EveTr	10.18140/FLX/1440132
CH-Oe1	47.2858	7.73194	450	1.2	2005 – 2008	2002 – 2004	30	34768	GRA	Grass	10.18140/FLX/1440135
DE-Gri	50.95	13.5126	385	3.0	2007 – 2014	2004 – 2006	30	34659	GRA	Grass	10.18140/FLX/1440147
DE-Hai	51.0792	10.4522	430	42.0	2005 – 2012	2002 – 2004	30	35028	DBF	DecTr	10.18140/FLX/1440148
DE-Kli	50.8931	13.5224	478	3.5	2007 – 2014	2004 – 2006	30	33933	CRO[2]	Grass	10.18140/FLX/1440149
DE-Lkb	49.0996	13.3047	1308	9.0	2012 – 2014	2009 – 2011	30	29726	ENF	EveTr	10.18140/FLX/1440214
DE-Obe	50.7867	13.7213	734	30.0	2011 – 2014	2008 – 2010	30	33872	ENF	EveTr	10.18140/FLX/1440151
FI-Hyy	61.8474	24.2948	181	24.0	2005 – 2014	2002 – 2004	30	30979	ENF	EveTr	10.18140/FLX/1440158
FR-LBr	44.7171	-0.7693	61	41.5	2005– 2008	2002 – 2004	30	34364	ENF	EveTr	10.18140/FLX/1440163
IT-Col	41.8494	13.5881	1560	32.0	2005– 2014	2002 – 2004	30	22918	DBF	DecTr	10.18140/FLX/1440167
IT-Sro	43.7279	10.2844	6	22.5	2005– 2012	2002 – 2004	30	26961	ENF	EveTr	10.18140/FLX/1440176
IT-Tor	45.8444	7.57806	2160	2.7	2008 – 2014	2008 – 2010	30	33126	GRA	Grass	10.18140/FLX/1440237
NL-Loo	52.1666	5.74356	25	26.0	2005– 2014	2002 – 2004	30	34098	ENF	EveTr	10.18140/FLX/1440178
US-AR1	36.4267	-99.42	611	2.8	2012 – 2012	2009 – 2011	30	35024	GRA	Grass	10.18140/FLX/1440103
US-CRT	41.6285	-83.3471	180	2.0	2014 – 2014	2011 – 2013	30	34895	CRO[3]	Grass	10.18140/FLX/1440117
US-Goo	34.2547	-89.8735	87	4.0	2005 – 2007	2002 – 2004	30	30848	GRA	Grass	10.18140/FLX/1440070

US-IB2	41.8406	-88.241	226.5	3.8	2005 – 2011	2004 – 2006	30	34339	GRA	Grass	10.18140/FLX/1440072
US-Me6	44.3233	-121.608	998	12.0	2013 – 2015	2010 – 2012	30	32141	ENF	EveTr	10.18140/FLX/1440099
US-MMS	39.3232	-86.4131	275	46.0	2005 – 2014	2002 – 2004	60	17508	DBF	DecTr	10.18140/FLX/1440083
US-Ne1	41.1651	-96.4766	361	3.0	2005 – 2013	2002 – 2004	60	17450	CRO[3]	Grass	10.18140/FLX/1440084
US-Ne2	41.1649	-96.4701	362	3.0	2005 – 2013	2002 – 2004	60	17407	CRO[4]	Grass	10.18140/FLX/1440085
US-Ne3	41.1797	-96.4397	363	3.0	2005 – 2013	2002 – 2004	60	17351	CRO[5]	Grass	10.18140/FLX/1440086
US-NR1	40.0329	-105.546	3050	21.5	2005 – 2014	2002 – 2004	30	35023	ENF	EveTr	10.18140/FLX/1440087
US-Oho	41.5545	-83.8438	230	32.0	2007 – 2013	2004 – 2006	30	31180	DBF	DecTr	10.18140/FLX/1440088
US-Syv	46.242	-89.3477	540	36.0	2005– 2014	2002 – 2004	30	27276	MF	DecTr	10.18140/FLX/1440091

290

Figure 2 *Location of FLUXNET sites (Table 3) coded by into three land cover types: deciduous trees (DecTr), evergreen trees (EveTr), and grass (Grass). Source of base map: OpenStreetMap (2017).*

3.2 MODIS LAI

The NASA Moderate Resolution Imaging Spectroradiometer (MODIS, (Nishihama et al., 1997)) four-day composite product MCD15A3H (Myneni et al., 2015) with 500 m resolution is treated as 'observed' LAI. Product data are available from 2002. We use the Fixed Sites Subsetting and Visualization Tool (ORNL DAAC 2018) for FLUXNET dataset to extract the MCD15A3H time series. To obtain a daily timeseries we linearly interpolate between values, for parameter derivation (Sect. 4.1).

3.3 Soil information

The SoilGrids (Hengl et al. 2014) database provides soil properties (i.e., organic carbon, bulk density, Cation Exchange Capacity (CEC), pH, soil texture fractions and coarse fragments) at seven depths (0, 0.05, 0.15, 0.30, 0.60, 1.00 and 2.00 m), as well as a bedrock depth prediction, World Reference Base (WRB) and USDA soil classes. We use the SoilGrids250m (Hengl et al. 2017) version, with its ~280 raster layers, to obtain the parameters (Table 4) to derive soil moisture deficit at wilting point ($\Delta\theta_{wp}$ in mm) for soil moisture related calculations (e.g. Eqn. 18).

The difference in soil moisture between field capacity (θ_{FC} in mm) and wilting point (θ_{WP} in mm) are used with parameters defined as (Saxon and Rawls 2006):

$$\Delta\theta_{\mathrm{wp}} = \theta_{\mathrm{FC}} - \theta_{\mathrm{WP}} = (W_{\mathrm{FC}} - W_{\mathrm{WP}})(1 - f_{CF})\, d_r \tag{23}$$

with

$$W_{\mathrm{FC}} = k_{\mathrm{FC}} + \left(1.283 \cdot k_{\mathrm{FC}}^2 - 0.374 \cdot k_{\mathrm{FC}} - 0.015\right) \tag{24}$$

using the weight fractions of sand f_{sand}, clay f_{clay} and f_{OM} organic matter

$$\begin{aligned} k_{\mathrm{FC}} = {} & -0.251 \cdot f_{\mathrm{sand}} + 0.195 \cdot f_{\mathrm{clay}} + 0.011 \cdot f_{\mathrm{OM}} \\ & +0.006 \cdot (f_{\mathrm{sand}}\, f_{\mathrm{OM}}) \\ & -0.027 \cdot \left(f_{\mathrm{clay}}\, f_{\mathrm{OM}}\right) \\ & +0.452 \cdot \left(f_{\mathrm{sand}}\, f_{\mathrm{clay}}\right) + 0.299 \end{aligned} \tag{25}$$

and

$$W_{\mathrm{WP}} = k_{\mathrm{WP}} + (0.14 \cdot k_{\mathrm{WP}} - 0.02) \tag{26}$$

where

$$\begin{aligned} k_{\mathrm{WP}} = {} & -0.024 \cdot f_{\mathrm{sand}} + 0.487 \cdot f_{\mathrm{clay}} + 0.006 \cdot f_{\mathrm{OM}} \\ & +0.005 \cdot (f_{\mathrm{sand}}\, f_{\mathrm{OM}}) \\ & -0.013 \cdot \left(f_{\mathrm{clay}}\, f_{\mathrm{OM}}\right) \\ & +0.068 \cdot \left(f_{\mathrm{sand}}\, f_{\mathrm{clay}}\right) + 0.031 \end{aligned} \tag{27}$$

Table 4 *Soil related parameters obtained from the SoilGrids (Hengl et al. 2014) database for each site (Table 3) at 250 m resolution for seven depths (Sect. 3.3). Values for each site (Table 3) are given in Sun et al. (2021).*

Parameter	Unit	Description
d_r	mm	Soil depth
f_{CF}	m m^{-3}	coarse fragment fraction
f_{clay}	kg kg^{-1}	clay fraction
f_{sand}	kg kg^{-1}	sand fraction
f_{silt}	kg kg^{-1}	silt fraction
f_{OM}	kg kg^{-1}	organic carbon fraction
ρ_{bulk}	kg m^{-3}	Bulk density

4 Parameter derivation for vegetated land covers: workflows and results

4.1 Leaf area index (LAI) and albedo related parameters

LAI is a key phenology parameter in SUEWS, it moderates albedo (α) and therefore surface radiative exchanges. LAI changes also modify both aerodynamic roughness parameters (roughness length z_0, zero plane displacement height z_d) (e.g. Kent et al. 2017) impacting aerodynamic resistance (r_a) and surface resistance (r_s). LAI directly moderates Q_E and canopy interception capacity, which modifies when potential evaporation occurs and aspects of the water balance.

As the SUEWS LAI equation (Eqn. 4) makes global optimisation techniques numerically challenging to derive all the required parameters, we take a two-step approach (Fig. 3):

1) Approximating growing stages using an asymmetric Tukey window function:

Tukey or cosine-tapered window (TW) is used in signal processing applications when data needs to be processed in short segments. It is defined (Bloomfield 2000):

$$TW(x,a)=\begin{cases}1 & (0<a<1\wedge a-2x-1\le 0\wedge a+2x-1\le 0)\vee(a=1\wedge x=0)\vee\left(a\le 0\wedge -\frac{1}{2}\le x\le\frac{1}{2}\right)\\ \frac{1}{2}(\cos(2\pi x)+1) & a>1\wedge -\frac{1}{2}\le x\le\frac{1}{2}\\ \frac{1}{2}\left(\cos\left(\frac{2\pi\left(-\frac{a}{2}+x+\frac{1}{2}\right)}{a}\right)+1\right) & 0<a\le 1\wedge x\ge -\frac{1}{2}\wedge a-2x-1>0\\ \frac{1}{2}\left(\cos\left(\frac{2\pi\left(\frac{a}{2}+x-\frac{1}{2}\right)}{a}\right)+1\right) & 0<a\le 1\wedge a+2x-1>0\wedge x\le\frac{1}{2}\\ 0 & |x|>\frac{1}{2}\end{cases} \quad (28)$$

where x is the independent variable and a the curve shape factor. We propose an asymmetric form of Tukey window (aTW) to approximate the intra-annual LAI dynamics:

$$aTW(x,a,b,x_0,l)=\begin{cases}\mathrm{TW}\left(\frac{x-x_0}{l},a\right) & x<x_0\\ \mathrm{TW}\left(\frac{x-x_0}{l},b\right) & x\ge x_0\end{cases} \quad (28)$$

where b is a curve shape factor for different segments, x_0 the segment parameter, and l the rescaling factor.

To demonstrate this we use the US-MMS site (Table 3), to fit the intra-annual LAI dynamics using an aTW curve (blue line, Fig. 4) to determine different phenological stages (shading, Fig. 4) and subsequently derive several related parameters:

- LAI_{min}: 5th percentile of LAI values before the growth and after the senescence
- LAI_{max}: 75th percentile of LAI values after the growth and before the senescence

- $T_{base,GDD}$: 99th percentile of air temperatures before the growth
- $T_{base,SDD}$: 10th percentile of air temperature after the growth and before the senescence.
- GDD_{full}: GDD at the end of growth based on $T_{base,GDD}$
- SDD_{full}: SDD at the end of senescence based on $T_{base,SDD}$
- α_{min} / α_{max}: 10th/90th percentile of daily albedo values after the growth and before the senescence. A daily albedo is calculated from 30/60 min FLUXNET observations of incoming and outgoing shortwave radiation for the period 10:00 to 14:00 (local standard time). To remove outliers a clustering method is applied (`ClusterClassify` of *Mathematica* v12.3.1 Wolfram Research 2020). For example, at some high-latitude sites (e.g. CA-Oas) snow occurs, the winter values are based on data from shortly after senescence to shortly before growth (next spring) and the clustering approach removes the snow period albedo values.

For evergreen and deciduous trees, $\alpha_{LAI,min}$ ($\alpha_{LAI,max}$) in Eqn. 6 typically corresponds to α_{min} (α_{max}), while for grassland a reverse relation holds (i.e. $\alpha_{LAI,min}$ corresponds to α_{max} and vice versa; see Cescatti et al. 2012 for a detailed analysis of albedo dynamics at FLUXNET sites).

2) Deriving curve factors used in SUEWS LAI scheme:

With the parameters derived in step 1, we can determine the curve factors $\omega_{1/2,GDD/SDD}$ by minimising the bias between MODIS observed (open triangle, Fig. 4) and SUEWS simulated (red line, Fig. 4) LAI values.

The derived LAI related parameters for the 38 FLUXNET sites vary between different land cover groups (Table 5, Fig. 5). The derived $LAI_{max/min}$ results are consistent with those reported in the literature (Asaadi et al. 2018). For EveTr sites, the large contrast between LAI_{max} and LAI_{min} in the ENF sites analysed here is consistent with MODIS derived LAI for ENF having larger seasonal variability than EBF (Heiskanen et al. 2012), but some of this is caused by a known issue of particularly low winter values (Garrigues et al. 2008).

Given the global availability of MODIS LAI and reanalysis-based air temperature datasets, we suggest the LAI related parameters be derived following this workflow (Fig. 3) to set parameters for SUEWS simulations. This can be done independent of the availability of flux tower observations.

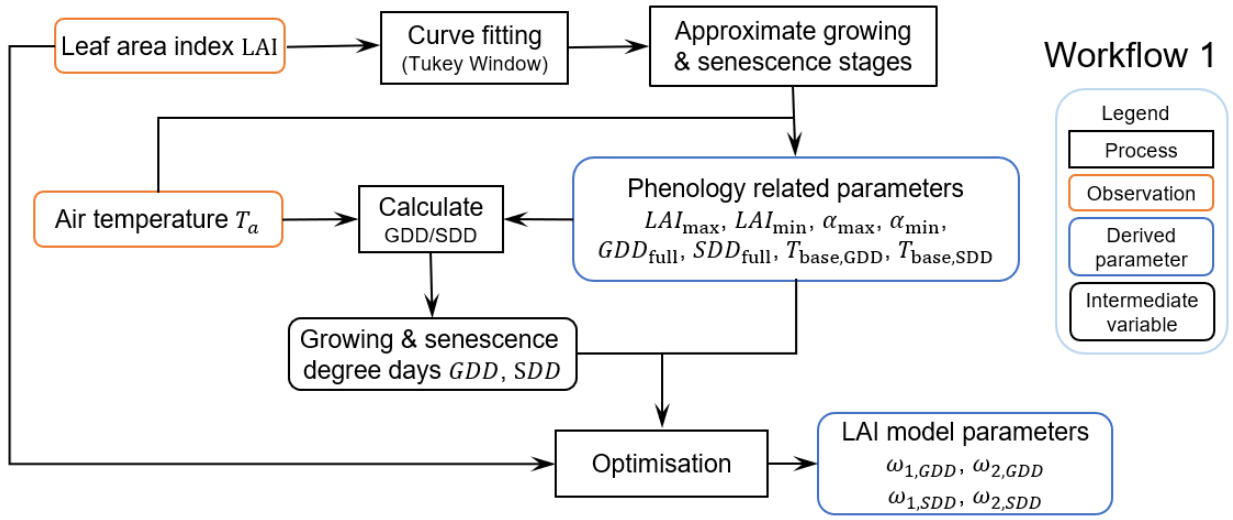

Figure 3 *Workflow 1 (Fig. 1) for deriving LAI and albedo related parameters. Related Jupyter notebooks are provided in Sun et al. (2021).*

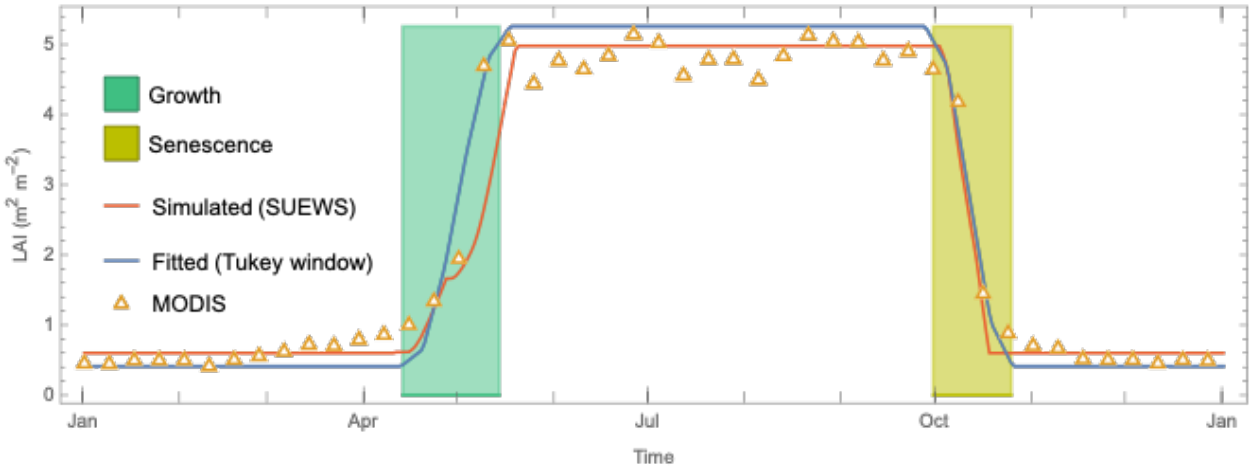

Figure 4 *Intra-annual LAI dynamics at US-MMS multi-year (2002–2014) ensemble median derived from MODIS observations (open triangle, Sect. 3.2) and simulated by SUEWS temperature-based LAI scheme (Eqn. 4) (orange line) with Tukey window fit (blue line, Sect. 4.1) using to derive the leaf-on or growth period (green shading) and senescence (yellow shading) periods.*

Table 5 *Inter-site variability within the three vegetation classes of LAI and albedo related parameters (Eqn. 4, Sect. 4.1) shown by mean and standard deviation. For individual site and by PFT type parameters see Appendix C (for digital version see Sun et al. 2021). Median and interquartile range (IQR) see Fig. 5.*

	α_{min} [-]	α_{max} [-]	LAI_{max} [m^2 m^{-2}]	LAI_{min} [m^2 m^{-2}]	GDD_{full} [°C day]	SDD_{full} [°C day]
EveTr	0.093±0.007	0.113±0.010	2.46±0.20	0.55±0.07	625±83	-501±87.
DecTr	0.102±0.004	0.125±0.006	2.9±0.4	0.66±0.07	475±137	-273±89.
Grass	0.156±0.007	0.185±0.009	2.15±0.13	0.35±0.06	484±102	-482±74.
	$T_{base,GDD}$ [°C]	$T_{base,SDD}$ [°C]	$\omega_{1,GDD}$ [-]	$\omega_{1,SDD}$ [-]	$\omega_{2,GDD}$ [-]	$\omega_{2,SDD}$ [-]
EveTr	2.8±1.2	12.5±1.2	-1.89±0.07	-0.0031±0.0006	0.00067±0.00023	0.96±0.31

DecTr	5.9±1.7	14.7±1.1	-1.54±0.20	-0.0043±0.0009	0.0018±0.0009	1.55±0.35
Grass	9.9±2.1	16.9±1.3	-1.93±0.04	-0.0031±0.0007	0.0012±0.0006	1.05±0.26

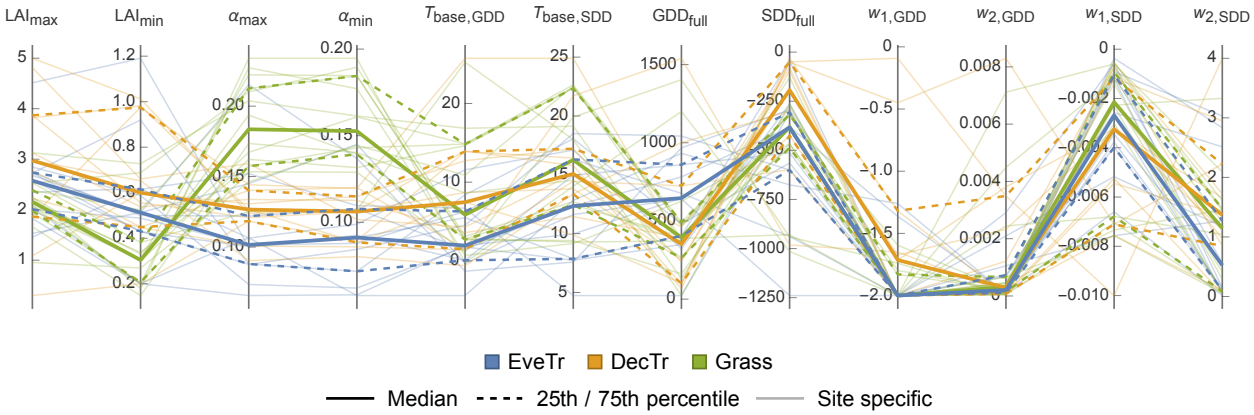

Figure 5 *Variation in LAI related parameters (Sect. 2.2.1) within three land cover classes (colour) showing median (thick line), interquartile range (IQR, 25th and 75th percentiles, dashed lines), site-specific values (thin lines).*

4.2 Storage heat flux coefficients

To calculate the storage heat flux ΔQ_S, the required OHM coefficients (Eqn. 7), can be determined from observed net all-wave radiation and observed storage heat flux, using ordinary linear regression. As the FLUXNET sites chosen are considered to be homogeneous, we derive coefficients for each site.

Ideally the storage heat flux measurements would include each of the components than are heating and cooling down on a daily basis, such as the soil, trunk, branches, leaves and air volume in a forest (e.g. McCaughey et al. 1985, Oliphant et al. 2004). However, these measurements are unavailable in the FLUXNET2015 dataset. Hence, we calculate a residual flux $\Delta Q_{S,res} = Q^* - (Q_H + Q_E)$ by assuming energy balance closure. This has the problem of accumulating the net measurement errors in this term (Grimmond et al. 1991, Grimmond and Oke 1999).

The derived OHM coefficients (Fig. 6) can be determined by season (Anandakumar 1999; Ward et al., 2016; Sun et al., 2017). We distinguish warm ("summer") and cold ("winter") seasons using months (summer: Northern Hemisphere JJA; Southern Hemisphere: DJF; winter: DJF (JJA), respectively). For simplicity, we omit periods when LAI may be changing rapidly. If the daily mean air temperature is warmer/cooler than the annual mean of daily median temperature, then summer/winter OHM coefficients are used in the simulations.

The OHM coefficients derived for the 38 FLUXNET sites (Table 6, Fig. 7) vary between land cover types and seasons. For each land cover type, a_1 and a_3 are notably larger in winter than in summer while the seasonal difference in a_2 is relatively small. Thus the overall fraction of heat stored does not vary much

but diurnal hysteresis effect is weaker in winter. These results are consistent with previous analytical results (Sun et al., 2017). Within each PFT, there is larger variability in a_2 and a_3 (cf. a_1), notably for evergreen and deciduous trees, suggesting using the most appropriate site values (e.g. medians) may improve predictions of the storage heat flux. In addition to the values derived here, we note that more detailed ΔQ_S observations are available for vegetated sites to derive such OHM coefficients (e.g. McCaughey (1985), Oliphant et al. (2004)).

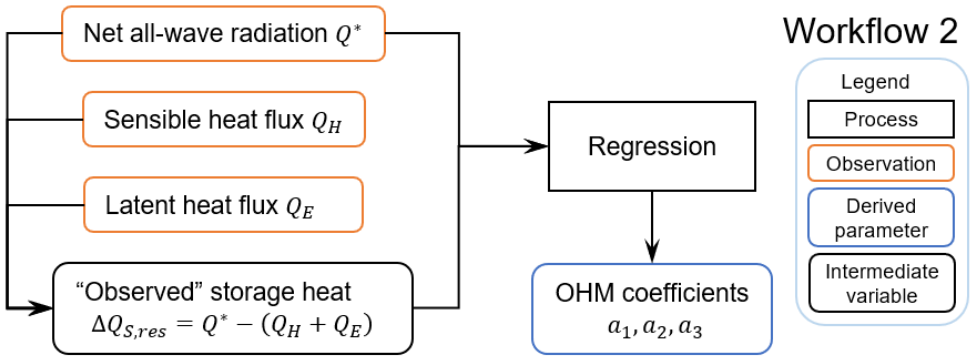

Figure 6 *Workflow 2 (Fig. 1) to derive OHM coefficients. Related notebooks are provided in Sun et al. (2021).*

Table 6 *As Table 5, but for OHM related parameters (Sect. 4.2). See Fig .7 for comparison and Table C2 for site specific values.*

	a_1 [-]		a_2 [h]		a_3 [W m^{-2}]	
	summer	**winter**	**summer**	**winter**	**summer**	**winter**
EveTr	0.294±0.027	0.49±0.04	0.140±0.023	0.110±0.021	-12.7±3.0	-4.8±2.8
DecTr	0.312±0.021	0.396±0.035	0.122±0.019	0.166±0.019	-12.9±2.8	-11.0±4.0
Grass	0.318±0.020	0.62±0.06	0.079±0.013	0.046±0.011	-14.9±2.0	-4.1±2.5

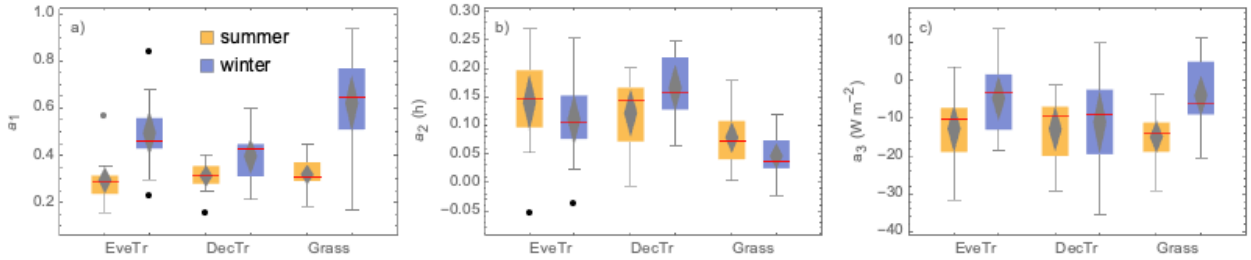

Figure 7 *Boxplots showing variability of OHM coefficients between land covers (EveTr, DecTr and Grass) and seasons (summer and winter): a) a_1 b) a_2 and c) a_3. Boxes (25th and 75th percentiles), whiskers (5th and 95th percentiles), with median (red line) and mean (middle grey diamond, with 95% confidence level (top and bottom) values, and outliers (dots).*

4.3 Surface conductance related parameters

As the Jarvis-type formulation of stomatal/surface conductance is widely used for many land cover types, many parameter sets exist (e.g. Stewart 1988; Grimmond and Oke 1991; Ogink-Hendriks 1995; Wright et

al. 1995; Bosveld and Bouten 2001; Järvi et al. 2011). Hoshika et al.'s (2018) comprehensive meta-analysis of published Jarvis-type stomatal conductance parameter values includes major woody and crop plants broadly similar to PFTs examined here.

Conventionally, the surface conductance parameters are derived by minimising the bias between the parameterised (Eqn. 14) and so-called "observed" values derived from an inverse form of Penman-Monteith equation (Eqn. 3):

$$\frac{1}{g_s} = r_s = \left[\frac{s}{\gamma}\frac{Q_H}{Q_E} - 1\right] r_a + \frac{\rho c_p VPD}{\gamma Q_E}. \quad (29)$$

This requires the surface be dry (Section 2.2.4) which we define as being without recorded rainfall in 24 h.

However, as the optimisation may not return values because of the complexity in Eqn. 14 and the challenge of interpreting the derived parameter values, we adopt Matsumoto et al.'s (2008) approach to derive these parameters. Rather than using all the data combinations for g_s, the upper boundary of each forcing variable component (e.g. $g(K_\downarrow)$) is considered as the response for unconstrained conditions. Specifically, the workflow is (Fig. 8):

1) Calculate aerodynamic resistance r_a (Eqn. 8) with roughness length z_{0m} and displacement height z_d derived from observed wind speed under neutral conditions (Appendix B).
2) Calculate "observed" surface conductance $g_{s,obs}$ (Eqn. 30).
3) Remove outliers from $g_{s,obs}$ data (step 2) iteratively (i.e. values larger than the 98th percentile until difference between 98th and 99th percentiles is < 1 mm s^{-1}). The remainder are used for deriving parameters.
4) Determine the upper boundaries of g_s curves with each component variable. To demonstrate this we use the US-MMS site (Fig. 9). First, original data are binned (sizes: 50 W m^{-2} for $K_\downarrow$, 2 °C for T_a, 2 kg kg^{-1} for Δq and 10 mm for $\Delta\theta$), the 95th percentiles of these bins are sampled 100 times (bootstrapped) to determine anchor points (red dots, Fig. 9). Second, the parameters are fit to the g_s related curves (Eqn. 14–17) using the anchor points using `NonlinearModelFit` of *Mathematica* v12.3.1 (Wolfram Research 2008).

The derived surface conductance parameters for the 38 FLUXNET sites (Table 7 and C3) have different intra-PFT variability based on the IQR (dotted lines, Fig. 10) and demonstrates the benefit of the observations and of deriving site-values when possible. It may help in selecting appropriate PFT from other sources (e.g. NOAH values in Appendix A). The g_{max} results are consistent with Hoshika et al. (2018) in terms of inter-PFT ordering (Grass > EveTr and DecTr). The grass and crop values are

457 comparable (Table C3) to Hoshika et al. (2018); however, our derived deciduous trees values are smaller
458 (22 cf. 31 mm s^{-1}) and evergreen trees values larger (20 cf. 12 mm s^{-1}).

459 A consistent $G_{q,shape}$ (eqn 16) value (0.9 units) is obtained for all sites, implying potential for
460 improvements to the $g(\Delta q)$ relation between g_s and Δq (e.g. other formulations $g_s(\Delta q)$ in Matsumoto et al.
461 (2008)) in future SUEWS development. This would be beneficial as there is a clear "plateau" observed
462 for low Δq (Fig. 9c). Similar issues are found in $g(\Delta\theta)$ for soil moisture related parameters. Although the
463 parameters derived here are the 'best' fit to the g_s forms in SUEWS v2020a, for each component variable
464 multiple g_s formulations exist with a range of variable fitting performance (e.g. Fig A1 in Ward et al.
465 2016). Here, we focus on *deriving the parameters* rather than *proposing new or more appropriate*
466 *formulations.*

467 Solar radiation related G_K parameter is linked to the level of incoming solar radiation needed for
468 evapotranspiration to occur. Given incoming solar radiation intensity varies with latitude, we see G_K
469 generally decreases polewards (Fig. 11a), suggesting geographical location could be used as a proxy for
470 deriving G_K.

471 The air temperature related G_T parameter indicates the optimal temperature for evapotranspiration to
472 reach its probable maxima. G_T appears to have a negative relation with latitude, but the two other
473 temperature parameters (T_L and T_H) have a very weak (none) with latitude (Fig. 11b). This suggests a
474 universal temperature range between T_L and T_H might be applicable across different sites while G_T should
475 be determined on a site-by-site basis.

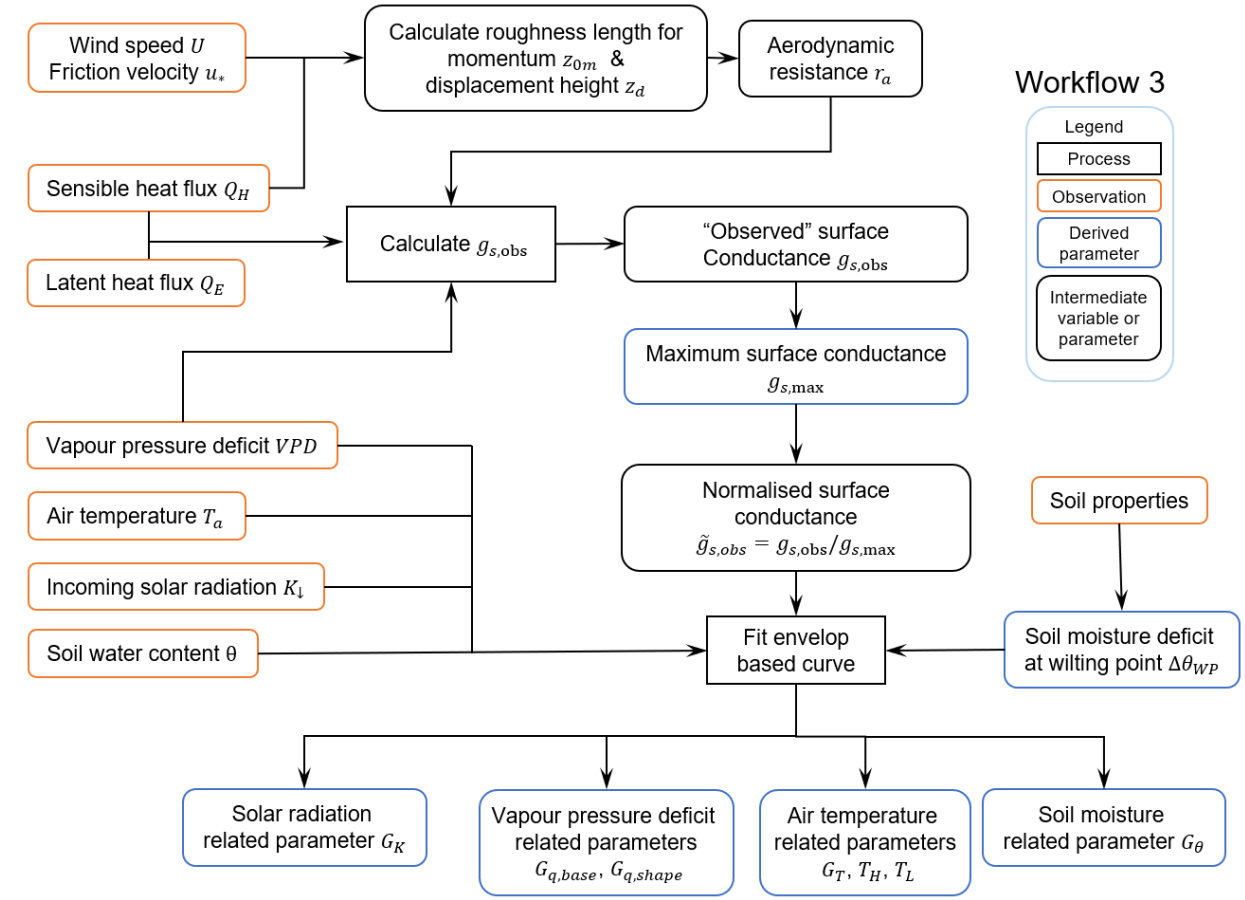

Figure 8 *Workflow 3 (Fig. 1) for deriving surface conductance related parameters. Related notebooks are provided in Sun et al. (2021).*

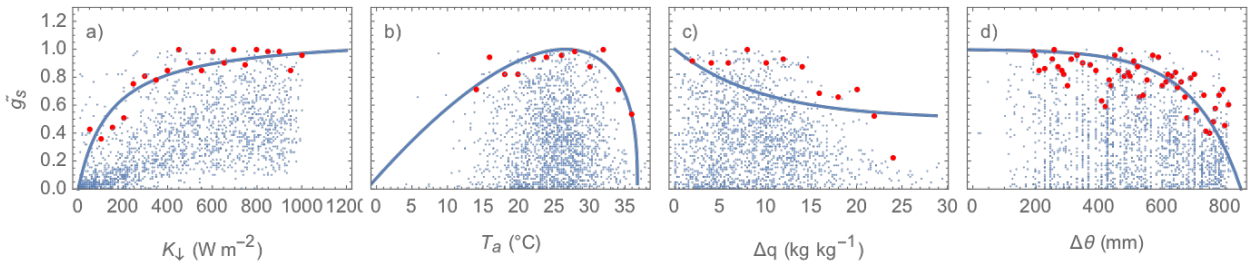

Figure 9 *Derived relations (blue lines) between normalised surface conductance $\tilde{g}_s$ and (a) incoming solar radiation $K_\downarrow$,(b) air temperature T_a, (c) specific humidity deficit Δq, and (d) soil moisture deficit Δθ based on anchor data points (red dots) after bootstrapping of observations (blue dots) for an example site (US-MMS).*

Table 7 *As Table 5, but for surface conductance related parameters (Sect. 4.3). See Fig. 10 and Appendix C.*

	g_{max} [mm s^{-1}]	G_K [W m^{-2}]	G_T [°C]	T_L [°C]	T_H [°C]	$G_{q,base}$ [-]	$G_{q,shape}$ [-]	G_θ [-]	$\Delta\theta_{WP}$ [mm]
EveTr	20.5±1.7	62±5	10.3±1.8	-13±4	41.4±2.0	0.391±0.033	0.9	0.033±0.009	511±75
DecTr	21.2±2.5	100±23	18.0±4.0	-18±5	38.0±1.5	0.439±0.024	0.9	0.029±0.010	521±58
Grass	38.6±2.8	87±13	26.1±1.9	-13±5	40.1±2.2	0.467±0.033	0.9	0.048±0.010	521±54

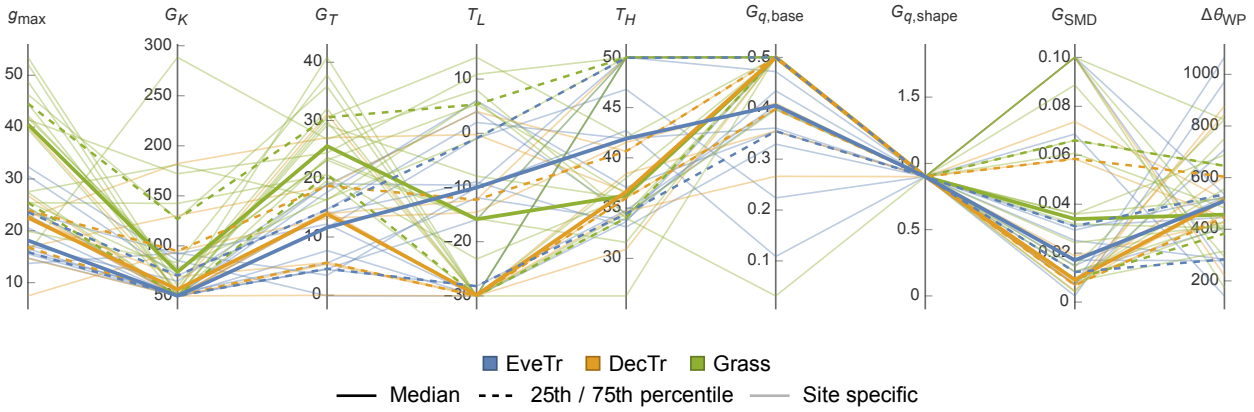

Figure 10 *As Fig.5, but for surface conductance related parameters.*

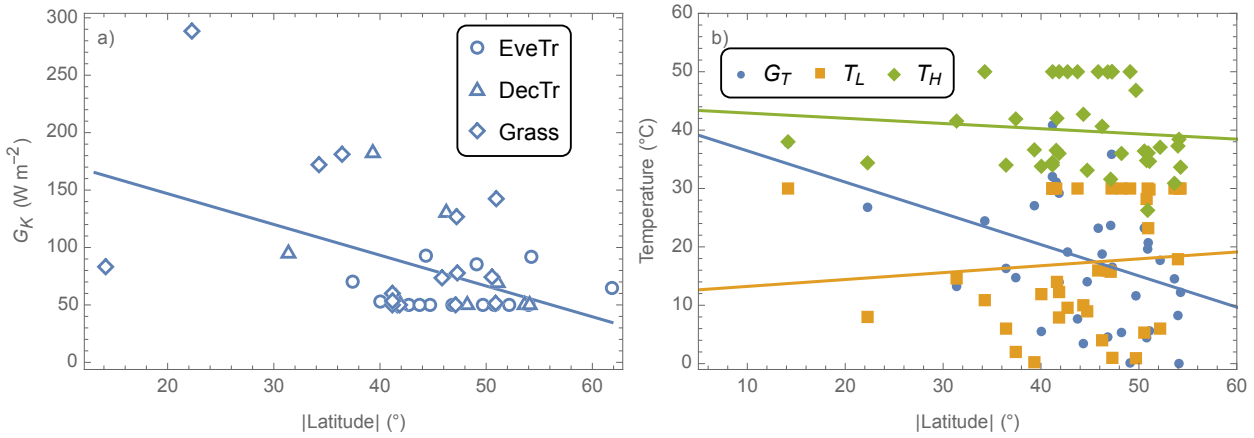

Figure 11 *Relations between absolute latitude and derived parameters: (a) solar radiation related G_K by PFT (symbol) and (b) temperature related G_T, T_L and T_H. Lines are derived by ordinary linear regression. See text for notation definitions.*

5 SUEWS performance in vegetated areas

5.1 SUEWS configuration and evaluation

SUEWS v2020a (Tang et al. 2021) is evaluated using its python wrapper SuPy v2021.3.18 (Sun and Grimmond 2019) with parameters (Table 1) and gap-filled 30/60 min meteorological forcing data (Table 2) based on FLUXNET2015 dataset. Simulations are conducted, with forcing data interpolated to a 5 min timestep (Ward et al. 2016), for three years (Table 3, *Evaluation period*) starting in mid winter. The first year is discarded to allow for model spin-up. The two subsequent years are evaluated when observed latent heat flux are available. In these model runs, the z_{0m} and z_{dm} values used are derived (Appendix B) by LAI state using observations for each LAI season for each (approximately 9 values per site; see Sun et al. (2021) for values). All other parameters (Table 1) are determined for the *parameter derivation period*

indicated in Table 3. At one site (AU-Gin), there are insufficient data for independent evaluation period from the parameter derivation period.

For the periods with 30(/60)-min Q_E EC observations (Y_{obs}) available, the 5 min simulated values (Y_{mod}) are averaged to 30(/60)-min to evaluate the j cases between 1 and the number of data points (N).The following metrics are used:

1) hit rate (HR):

$$\mathrm{HR} = \frac{\sum_{j=1}^{N} H(\delta_{Y,j} - |Y_{\mathrm{mod},j} - Y_{\mathrm{obs},j}|)}{N} \tag{30}$$

with Heaviside step function H defined by

$$H(x) = \begin{cases} 0, & x < 0 \\ 1, & x \geq 0 \end{cases} \tag{31}$$

and the threshold $\delta_{Y,j}$ being a value dependent on evaluation variable Y.

In particular, $\delta_{Y,j}$ for Q_E is determined as a function of net all-wave radiation Q^* following Hollinger and Richardson (2005) to be $\delta_{Y,j} = 0.1Q_j^* + 10$ (in W m^{-2}) based on measurement uncertainties.

2) mean absolute error (MAE):

$$\mathrm{MAE} = \frac{\sum_{j=1}^{N} |Y_{\mathrm{mod},j} - Y_{\mathrm{obs},j}|}{N} \tag{32}$$

3) mean bias error (MBE):

$$\mathrm{MBE} = \frac{\sum_{j=1}^{N} (Y_{\mathrm{mod},j} - Y_{\mathrm{obs},j})}{N} \tag{33}$$

Both the MAE and MBE would ideally be 0 (with units of parameter/variable assessed). Whereas if the HR=1 it indicates all model predictions fall within the acceptable threshold set, while HR =0 would suggest none are within the acceptance threshold.

A performance score PS as a function for each metric (x; i.e. HR, MAE, |MBE|) is used to rank the sites:

$$PS = \frac{1}{N} \sum_{k=1}^{N} (w_x \tilde{x})_k \tag{34}$$

where $\tilde{x}$ is the rescaled ranking score a given metric after being ranked from poorest to best and w_x is a weight associated with the temporal analysis type k which varies from 1 to N (number of component periods; e.g., N = 24 for hourly results). Equal weights (1/3) are used in the PS calculations for HR, MAE and |MBE|.

5.2 Impacts of model parameters on model performance

Given the many parameters in SUEWS, first we assess the relative importance of the parameters. We assume in this analysis our derived parameters (Sect. 4) are "perfect", so we can undertake a sensitivity analysis (McCuen 1974, Beven 1975) of the Penman-Monteith equation (i.e. Eqn. 3, denoted by PM hereafter):

$$\Delta Q_E = PM(AE + \Delta AE, r_a + \Delta r_a, r_s + \Delta r_s) - Q_E \quad (35)$$

where $AE = Q^* - \Delta Q_S$ is the available energy, incorporating parameters influences related to LAI, albedo and OHM. Similarly, multiple parameters influence the resistance terms. In Eqn. 31 the prefix Δ indicates bias terms. For simplicity, we consider the direct impacts only (i.e., secondary impacts from parameters inter-dependence are ignored). Expanding Eqn. 31 in Taylor series, gives:

$$\Delta Q_E \approx PM'(AE) \cdot \Delta AE + PM'(r_a) \cdot \Delta r_a + PM'(r_s) \cdot \Delta r_s \quad (36)$$

where $PM'(x)$, the first-order derivative of x, indicates the sensitivity of modelled Q_E. Note "≈" implies the approximation of ΔQ_E as the sum of bias from the chosen parameters. To examine the influences of different parameters in model performance, we use two non-dimensional metrics derived from Eqn. 32:

1) *sensitivity coefficient* (SC) (McCuen 1974):

$$SC = PM'(x) \cdot \frac{x}{Q_E} = \frac{\partial Q_E}{\partial x}\frac{x}{Q_E} \approx \frac{\Delta Q_E / Q_E}{\Delta x / x} \quad (37)$$

   gives the fractional change in x causing a change in Q_E, indicating a relative sensitivity of PM to x. For instance, SC= 0.5 suggests a 20% increase in x may increase Q_E by 10% (=20% × 0.5).

2) *attribution fraction* (AF): quantifies the fraction of model bias derived from a given parameter x:

$$AF = PM'(x) \cdot \frac{\Delta x}{\Delta Q_E} \quad (38)$$

   Ideally, the sum of all AF contributors would equal one, but as we omit inter-dependence of impacts of parameters, this may not occur. However, comparing the different contributors is indicative of their relative importance in modelled Q_E.

For both SC_{AE} and SC_{r_a} they are generally a similar type of patterns (Fig. 12a-f) with seasonal and diurnal variations for the three PFT. During warm periods (~summer and ~noon time), with an increase in ΔAE and Δr_a it is found to lead to larger positive bias in modelled Q_E; whereas in cooler periods (~winter and ~night time) the ΔAE and Δr_a is found to increase the negative bias.

However, the temporal patterns in SC_{r_s} differ (Fig. 13g-i) from those in SC_{AE} (Fig. 13a-c) and SC_{r_a} (Fig. 13d-f): the SC_{r_s} values are always negative, and consistently larger in magnitude (cf. SC_{AE} and SC_{r_a}), implying a particularly strong sensitivity of Q_E to r_s. This is consistent with Beven (1975), who found it to dominate the modelled summertime Q_E sensitivity in the PM framework.

The relative (cf. total) bias from the parameters is assessed in modelled Q_E at monthly and hourly temporal scales using the median AF (Fig. 13). AF_{r_s} is larger than both AF_{AE} and AF_{r_a}; i.e., r_s imposes a dominant influence in modelled Q_E bias. There is more temporal variability in AF_{r_s} (cf. AF_{AE} and AF_{r_a}) with cooler periods (morning and evening, whole winter) generally have values greater than one, indicating the bias in r_s dominates modelled Q_E. As AF_{r_s} is still generally larger than ~0.3 (except for transitional periods in summer, 8:00–9:00 in the morning, when $AF_{r_s} < \sim 0.3$), r_s remains an important control on modelled Q_E. These results together, indicate that it is critical to assign accurate r_s to obtain accurate estimates of Q_E.

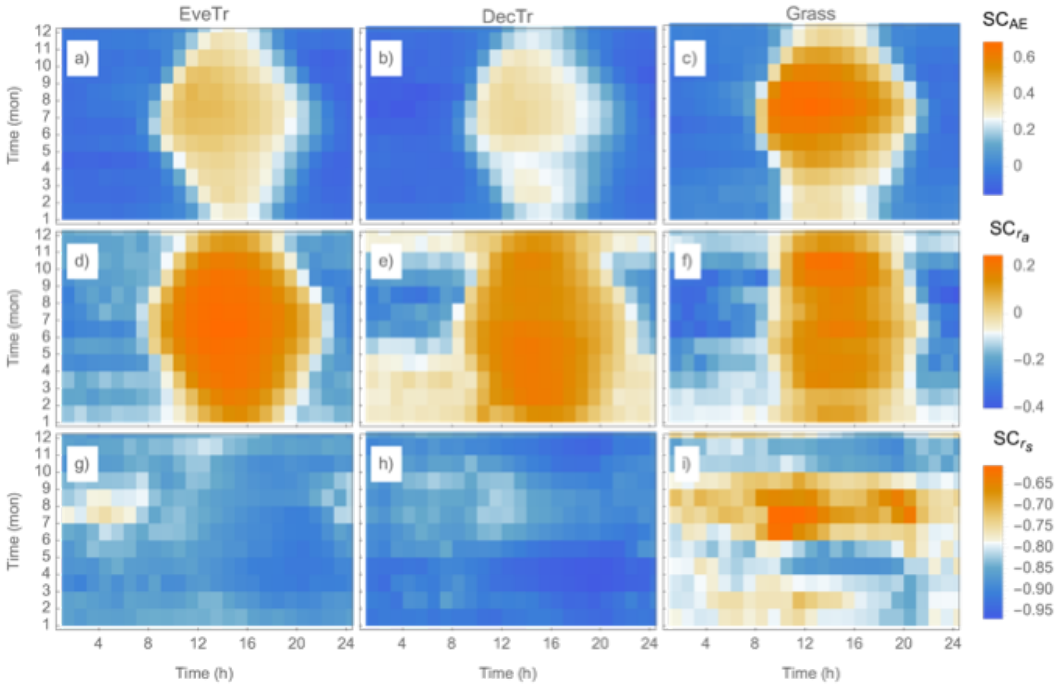

Figure 12 *Temporal variation in median (colour) sensitivity coefficient (SC, eq.38) of (a-c) available energy (AE, sect. 5.1), (d-f) aerodynamic resistance (r_a) and (g-i) surface resistance (r_s) for (a,d,g) evergreen trees (EveTr), (b,e,h) deciduous trees (DecTr), and (c,f,i) grassland and crops (Grass).*

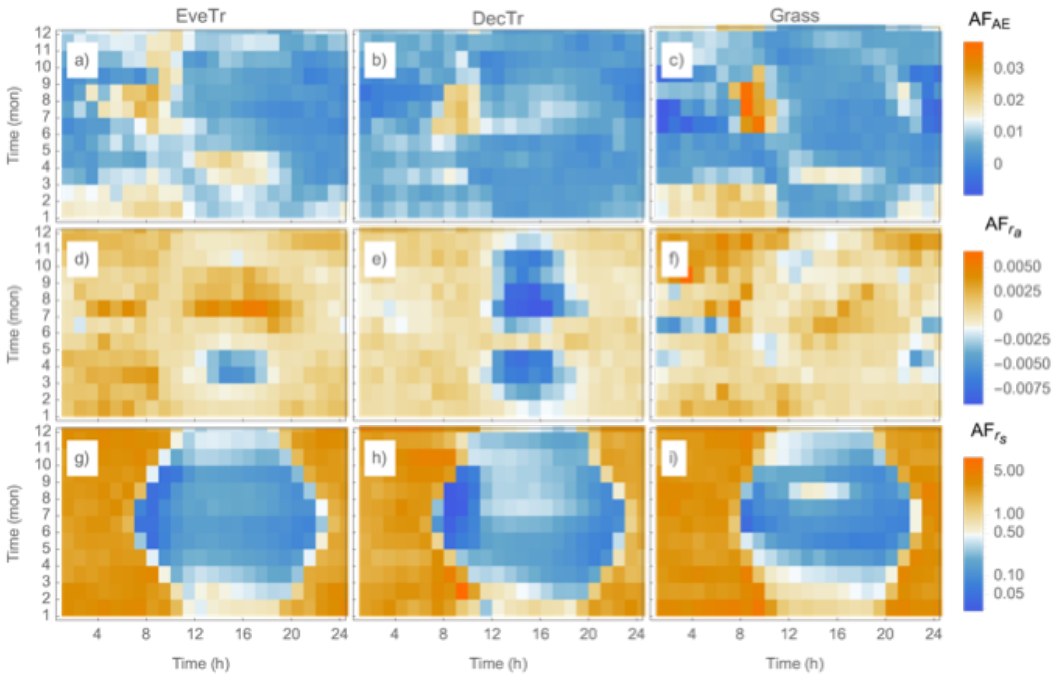

Figure 13 *As Fig.12, but the attribution fraction (AF, Eq. 39). Note AF_{rs} scale is logarithmic.*

5.3 Evaluation of SUEWS simulated Q_E with two different sources of g_s parameters

Given the critical importance of surface resistance to model performance in Q_E (Sect. 5.2), we assess the impact two different sources of g_s parameters (keeping all other site parameters the same, with the values as indicated in section 5.1): (i) site-specific values derived from FLUXNET2015 data (Sect. 4); and (ii) PFT-specific NOAH values modified for SUEWS (Appendix A). Errors in the other derived parameters (e.g., LAI related parameters, storage heat flux coefficients via available energy) will impact both sets of results but they are assumed to be equal, allowing the impacts of using site- and PFT-specific g_s parameters on SUEWS simulated Q_E to be assessed. Given NOAH is extensively used in NWP systems (e.g., WRF, Skamarock and Klemp, 2008), the result also allows the applicability of NOAH-based g_s parameters at FLUXNET sites to be assessed.

Analysis using two years of Q_E EC flux data (after 1 year spin up) uses three metrics (Sect. 5.1). The overall median results are similar between the two sets of parameters across the 38 sites split into the three PFTs (Fig. 14, red lines). The median HR are between 0.6 and 0.7, median MAE are less than 25 W m^{-2}, and median MBE are ~5 W m^{-2}. The Grass site, notably HR and MAE (Fig. 14a, b), performance is very similar suggesting the NOAH-based parameters could be used for these sites at annual scales as a first-order proxy.

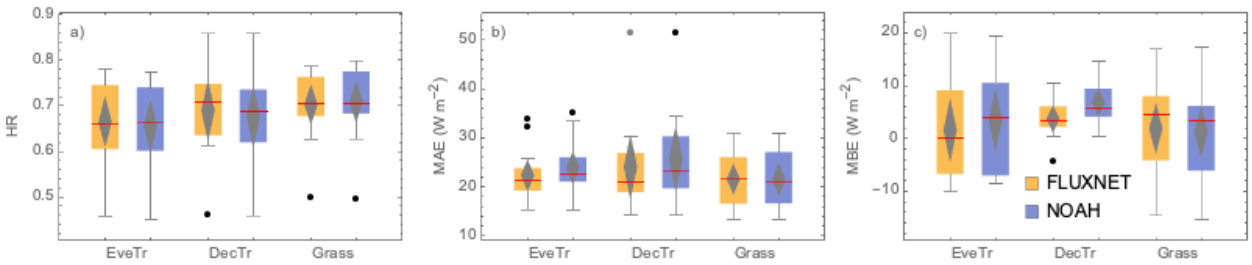

588

589 ***Figure 14*** *Simulated Q_E using two sets of parameters (colour, FLUXNET - Table C3, NOAH – Table*
590 *A1 assigned based on Table 3 PFT class) at 38 sites (boxplots, as Fig. 9, subdivided into three*
591 *land cover classes: EveTr, DecTr and Grass) evaluated for two years with observed 30/60-min*
592 *fluxes using three metrics (Sect. 5.1): (a) HR, (b) MAE, and (c) MBE.*

593 Evaluation using three different time periods (annual, monthly and hourly), shows differences in
594 performance between using the FLUXNET2015 and NOAH-based parameters (Fig. 15). The HR is
595 similar for all three temporal scales (Fig. 15a–c) for the three site types (colour). Both the MAE (Fig.
596 15d–f) and MBE (Fig. 15g–i) indicate better model performance can be obtained using the
597 FLUXNET2015-based parameters (i.e. not above the 1:1 line). When using the NOAH parameters (Fig.
598 15h,i), some monthly MBE are ~40 W m^{-2} larger at EveTr sites for 8 of 156 cases and 5/312 for DecTr
599 sites. Similarly, at the hourly scale the NOAH MBE are on occasions ~30 W m^{-2} larger (4/132 EveTr
600 cases and 6/264 DecTr cases). However, the NOAH results have similar metrics at Grass sites. This
601 suggests at the EveTr and DecTr sites, the NOAH-based g_s parameters may on occasion be less
602 appropriate, suggesting that the individual sites values may be better.

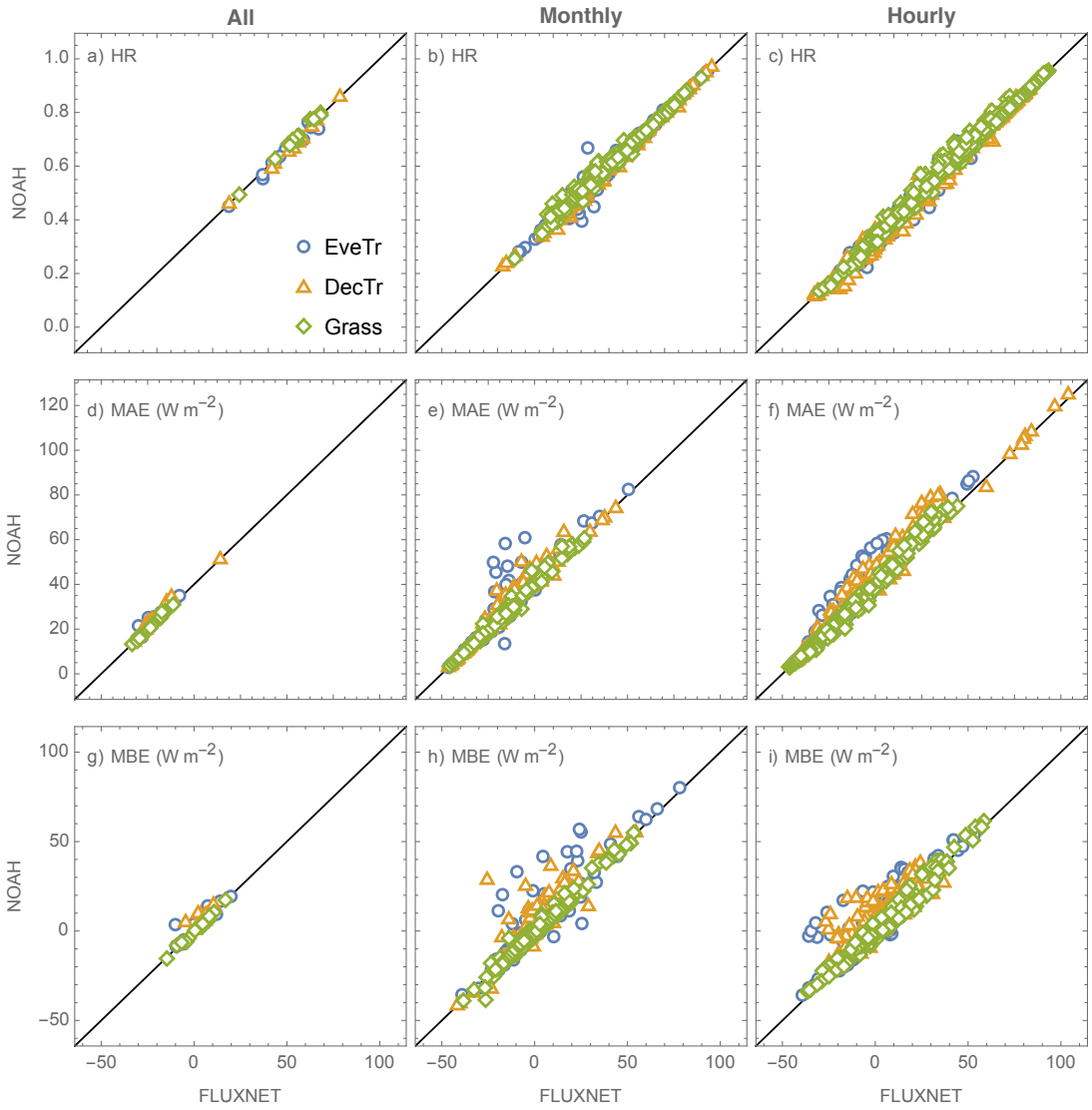

Figure 15 *As Fig 14, but evaluation metrics (colour coded by land cover class) determined for three temporal scales (columns): (a,d,g) whole period (n = 38 sites but different number of samples per site, Table 3), (b,e,h) monthly (n = 456 = 38 sites × 12 months) and (c,f,i) hourly (n = 912 = 38 sites × 24 hours) ,*

5.4 Evaluation of SUEWS simulated Q_E and key parameters at sites with contrasting model performance

Given the results in Section 5.3, the performance of individual sites using the FLUXNET2015-derived parameters (Sect. 4) at monthly (Fig. 16) and hourly (Fig. 17) time scales are investigated.

As expected (Sect. 5.2), the HR values are consistently better at all sites during cooler (winter) than warmer (summer) seasons (Fig. 16a–c), and similarly for night rather midday time periods (Fig 17a–c). Given the consistency in MAE and HR (Fig. 16,17d-f) patterns, the sites identified to be simulated the 'best' (blue) and 'poorest' (orange) are the same (Section 5.1).

However, using the MBE different sites are selected. For example, monthly MBE at AU-ASM stays close to zero throughout the year while at AU-Das it varies between -40 W m^{-2} and 60 W m^{-2} (Fig 16h). The largest intra-month MBE range for an EveTr site is 87.1 W m^{-2}, which occurs at FR-LBr. The equivalent range for DecTr sites is larger (96.1 W m^{-2} at AU-DaS) but smaller at Grass sites (69.6 W m^{-2}; US-Ne3). The intra-hourly MBE ranges are smaller than intra-monthly values: with a DecTr and a Grass site having a large range than the largest EveTr site (AU-DaS (61.9 W m^{-2}), US-Goo (60.0 W m^{-2}), FR-LBr (53.1 W m^{-2}), respectively).

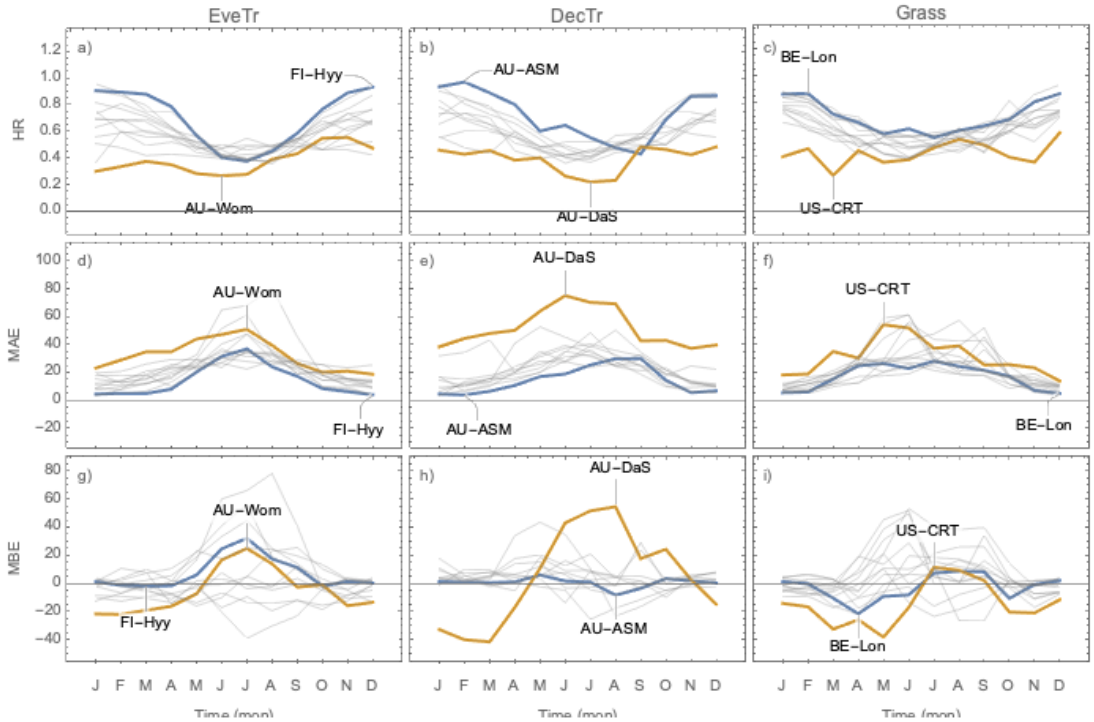

Figure 16 *Variation in evaluation metrics (Section 5.2) based on 30/60-min Q_E data by month using the derived parameters based on FLUXNET2015 dataset (Tables C1–C3): (a–c) HR, (d–f) MAE, (g–l) MBE by sites grouped into three PFTs (a,d,g) EveTr, (b,e,h) DecTr and (c,f,i) Grass with sites of best (blue)/poorest (orange) performance highlighted while others in grey (indicated by PS: see text and Eqn. 35 for details). Note Southern Hemisphere sites are offset by 6 months (Sect. 5.1), so 'general' seasons are consistent across sites.*

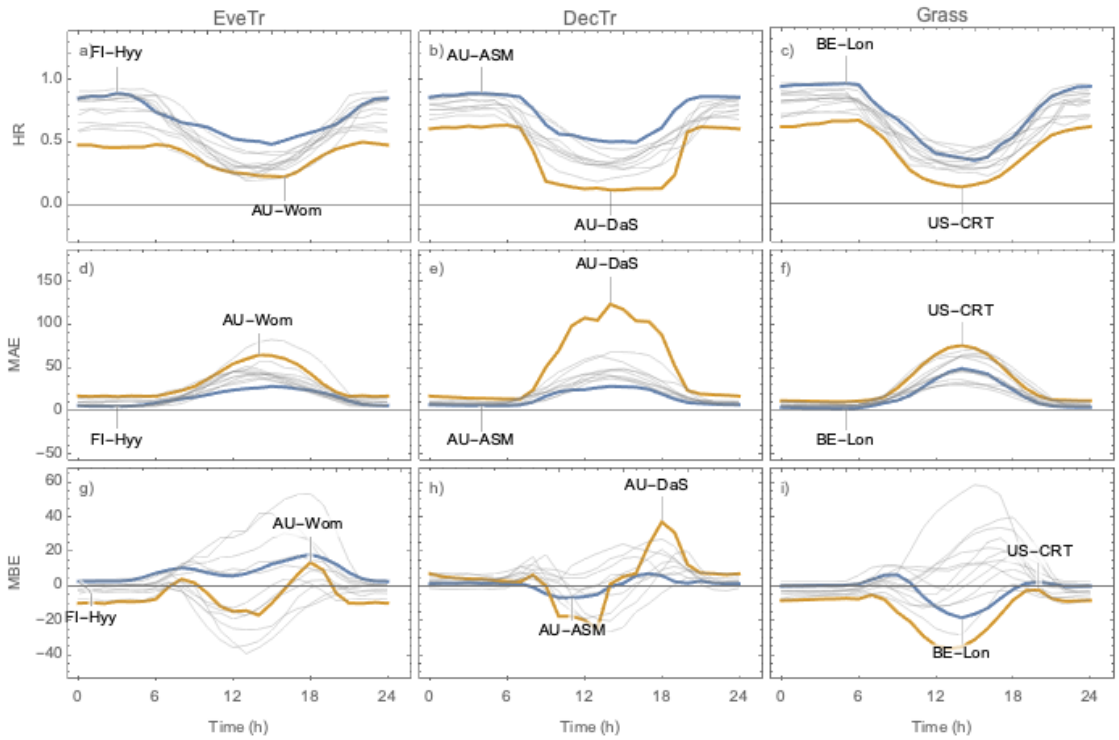

Figure 17 *As Fig. 16, but for diurnal cycles using local standard time.*

To investigate Q_E performance relative to key parameters (LAI, r_a, and g_s) we select the sites with contrasting results from each PFT to understand the drivers. The hourly and monthly ranked performance (Eqn. 35) are broadly consistent within each PFT type (Fig. 18). Sites with higher hourly scores generally have better monthly scores, except for IT-SRo within the EveTr cohort. It has the highest hourly PS (0.86) but is ranked fourth based on $PS_{monthly}$ (0.64), whereas the highest $PS_{momthly}$ (0.91) is for FI-Hyy which also has the second rank PS_{hourly} (0.83). To select sites for further analysis we rank based on the mean of monthly and hourly PS results. The six sites chosen are the best and poorest sites for the three PFTs (i.e. extremes in Fig. 18, highlighted in Fig. 16 and 17).

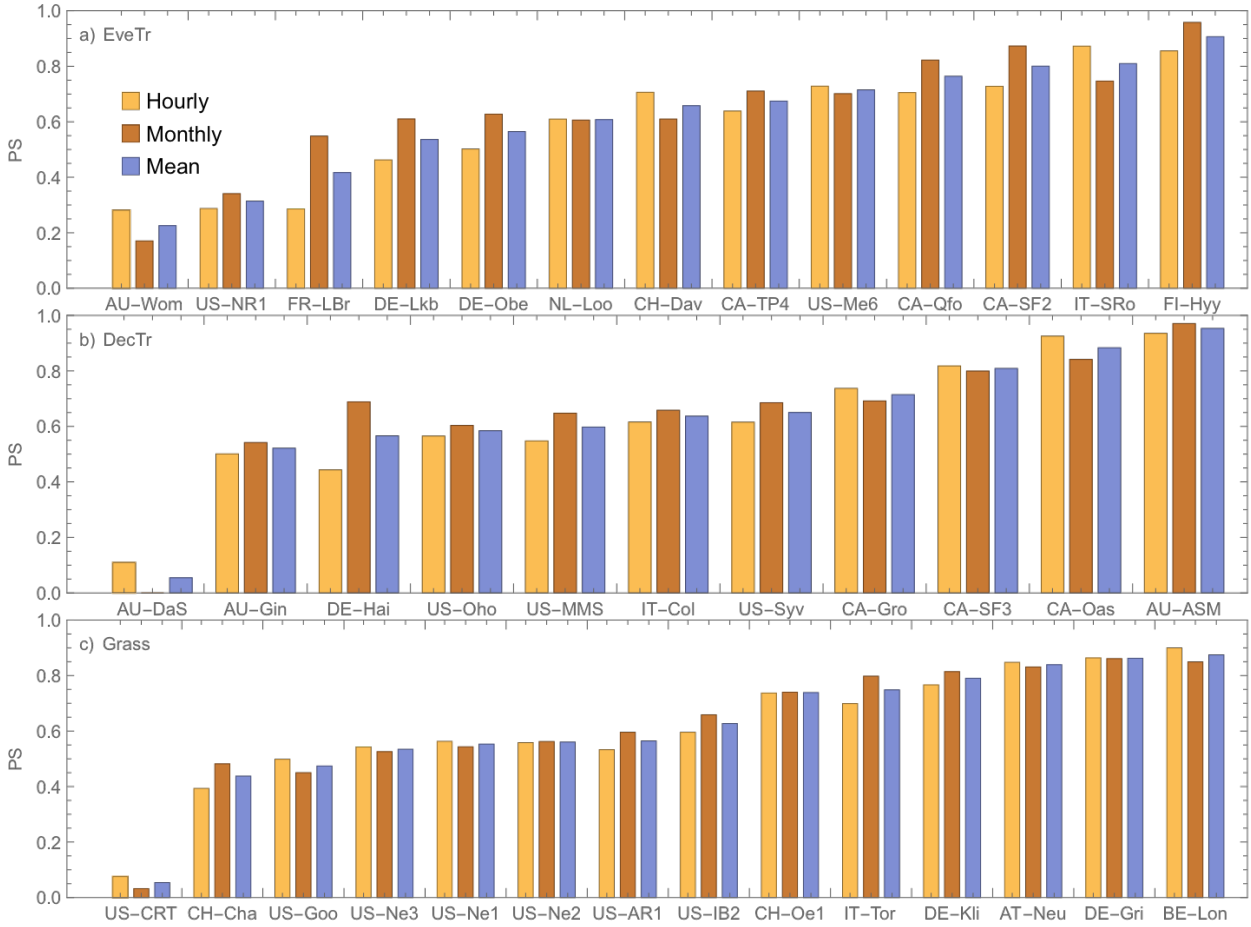

Figure 18 *Performance score (PS, Eqn. 35, higher value better) using FLUXNET2015 derived parameters for sites (Table 3) from three PFT: a) EveTr, b) DecTr and c) Grass.*

Comparing the contrasting site Q_E performance (best cf. poorest) for the three PFTs (Fig. 19 cf. 20; 21 cf. 22; 23 cf..24), we identify the skill of capturing the annual LAI dynamics is crucial to seasonal model performance (Fig. 19–24a). At the "best" sites but BE-Lon (a Grass site, whose performance is more controlled by surface conductance g_s skill and shall be discussed later) the phenology generally has the correct timing while at the poorest onsets of some stages are missed (e.g. Fig 22a). Timing appears to be more critical than magnitude, as although the LAI magnitude at AU-ASM has a large bias in year 2 (0.5 m^2 m^{-2}, Fig. 21a) the phenology timing is well captured. This result for a first rank site (i.e. best performance) implies the rescaling nature of LAI in parameterisation of albedo (Eqn. 6) and surface conductance (Eqn. 14) plays an important role. This indicates the importance of assigning appropriate LAI parameters, notably those influencing the timing (i.e. temperature thresholds $T_{base,GDD}$ and $T_{base,SDD}$ in Eqn. 4), in SUEWS modelling Q_E at vegetated sites.

As expected (Sect 5.2), SUEWS performance is critically impacted by surface conductance g_s skill (Fig. 19–24b–e *cf.* j–m): sites and seasons with better model g_s skill (i.e. simulations and observations closer) show overall better performance (e.g. for Grass sites, BE-Lon vs. US-CRT, cf. Fig. 23c and 24c). g_s is better modelled in warmer (JJA and SON) than cooler seasons (MAM and DJF). At night, g_s is generally underestimated, by a similarly order of magnitude as that in cooler seasons (~3 mm s^{-1}). These results, consistent with SUEWS results for two UK urban sites (Ward et al 2016), suggest improvements are needed in the Jarvis type g_s parameterisation during cooler periods. Given the method adopted here of using summertime observations, as used by many other land surface models (e.g. NOAH - Chen and Dudhia 2001; HTESSEL - Balsamo et al. 2009), it implies that the widely adopted Jarvis type g_s parameterisations and/or related parameter values (cf. Sect. 4.3) maybe biased towards vegetation canopies in warmer periods. The "cool" bias in modelled g_s found here, and in earlier SUEWS work (e.g., Ward et al. (2016)), should be considered a more common issue beyond the SUEWS model. Given the needs in long-term climate modelling, systematic biases should be removed suggesting other land surface models that adopt the Jarvis type g_s parameterisation might need revisions as well.

The aerodynamic resistance r_a is modelled well at all sites (Fig. 19–24f–i), with nocturnal biases larger (e.g. underestimate of ~50 s m^{-1} at AT-Neu, Fig. 23f–i). This good performance may be largely attributed to the use of local site - growth stage derived aerodynamic roughness parameters (Appendix B) rather than estimated using a morphometric model (e.g. based on canopy height). To estimate z_{0m} and z_d using Eqn. 9 and 10 the f_0 and f_d parameters can be derived using Sun et al. (2021) for different growing stages with the FLUXNET2015 data when canopy heights are available. The largest intra-PFT variability, occurs for 'Grass' sites (Fig. B1).

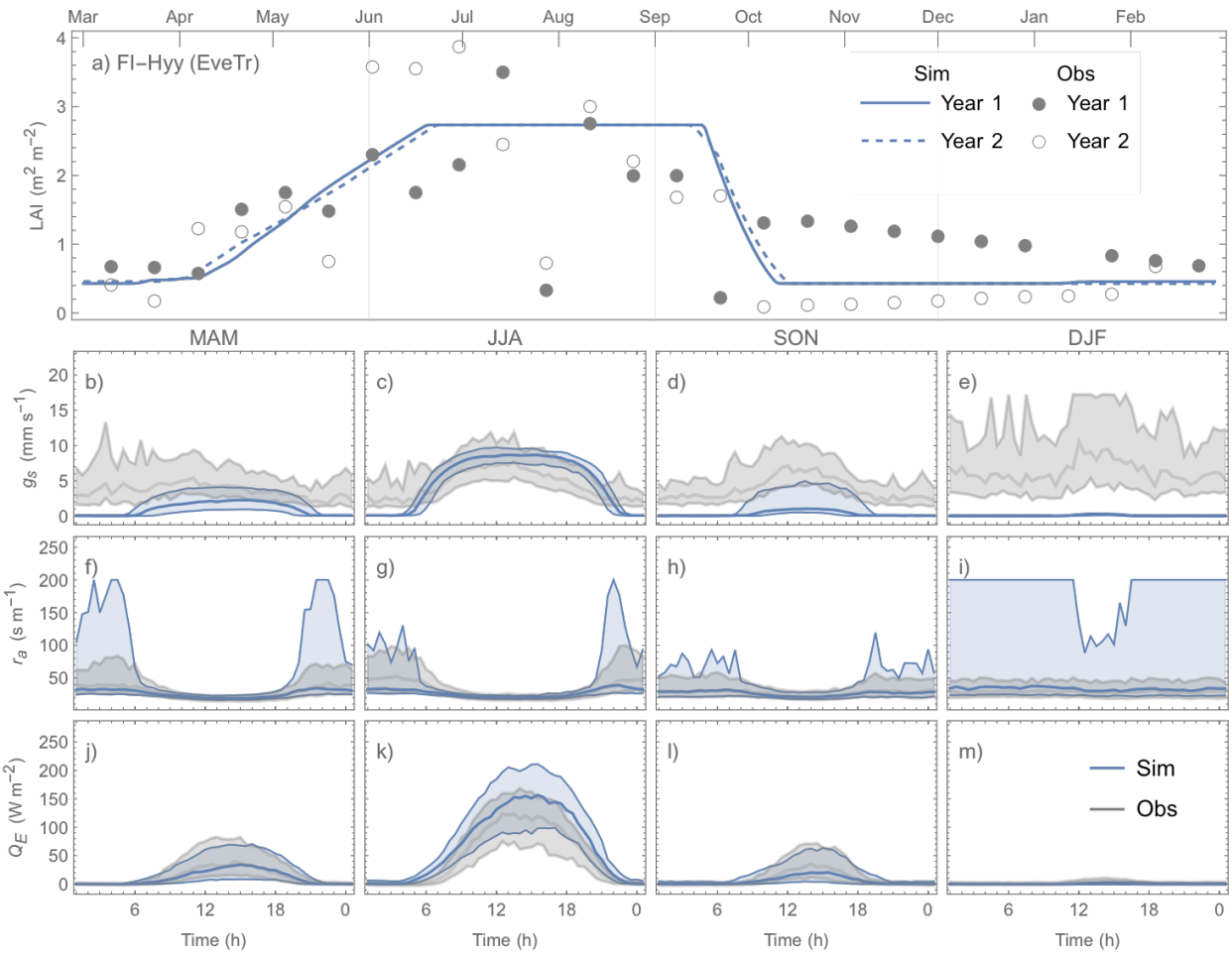

Figure 19 *FI-Hyy (EveTr, PS=0.92) performance (a) annual LAI. (b–e) g_s (in seasonal ensemble of diurnal cycles: median values in bold lines, while interquartile ranges in shadings), f–i) r_a; and j–m) Q_E. Note the same colouring of simulations for sites with best/poorest model performance and six-month offset in annual cycles are applied for consistency with Fig. 16 and 17.*

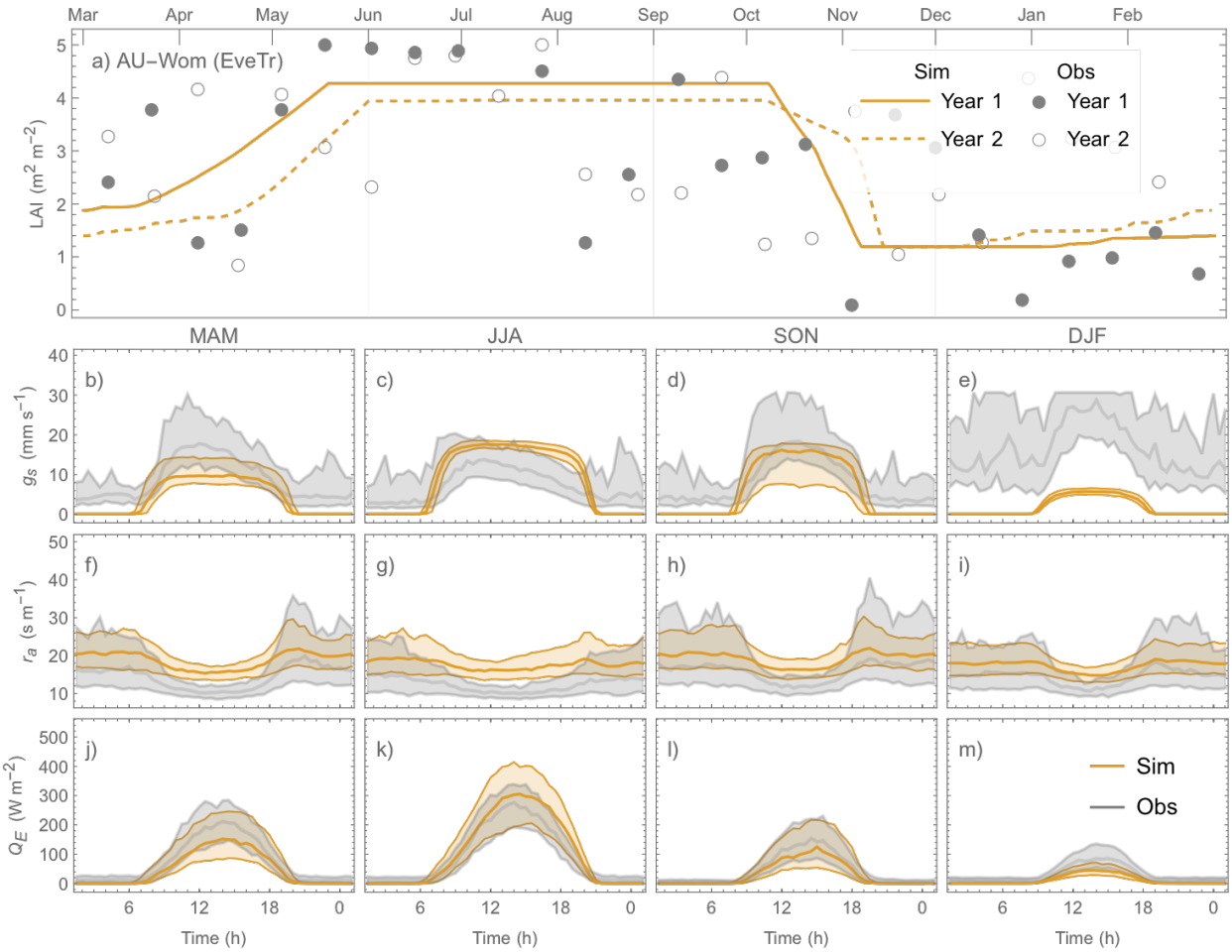

Figure 20 *As Fig. 19, but for AU-Wom (EveTr, PS=0.18).*

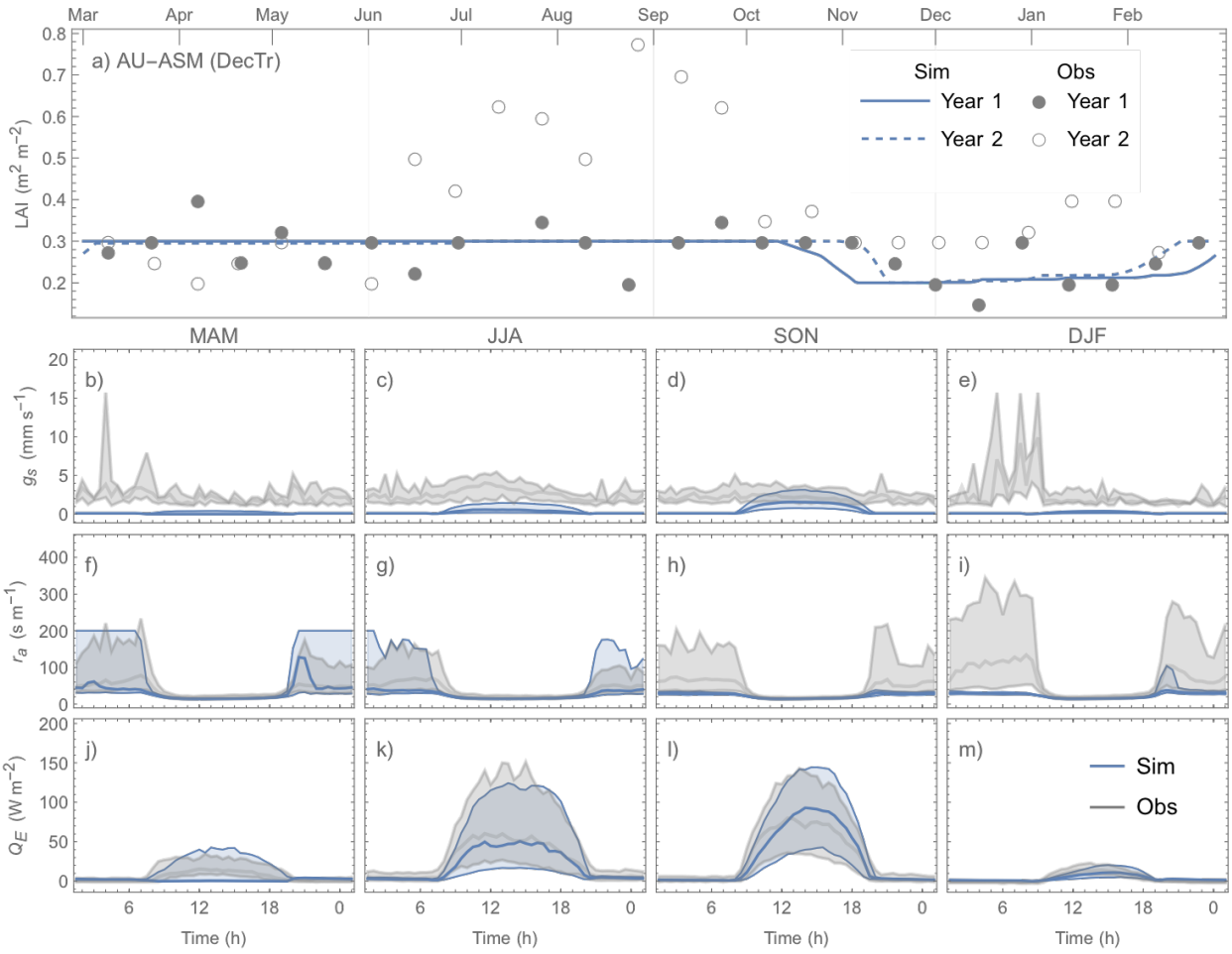

Figure 21 *As Fig. 19, but for AU-ASM (DecTr, PS=0.96).*

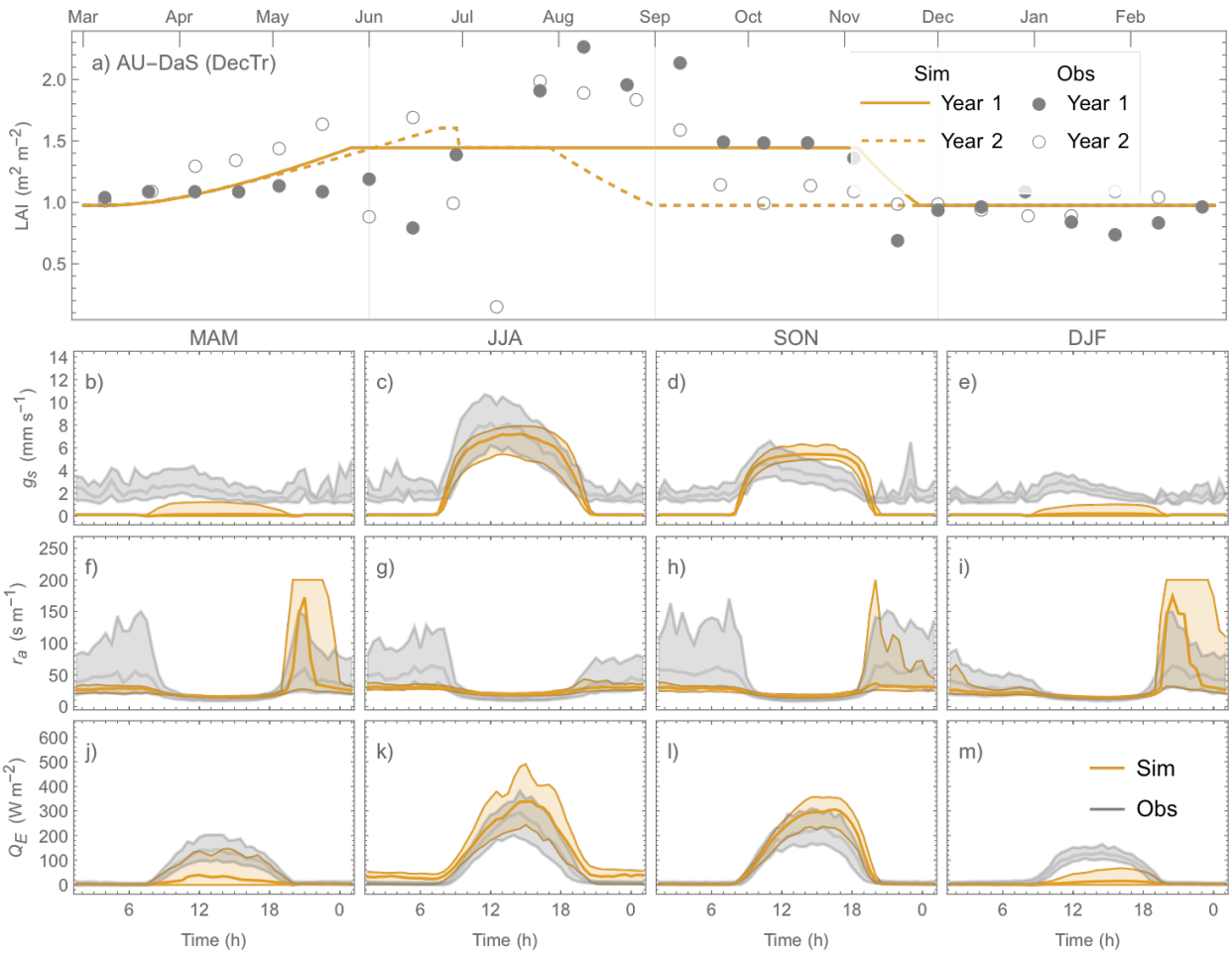

690

691 ***Figure 22*** *As Fig. 19, but for AU-DaS (DecTr, PS=0.04).*

692

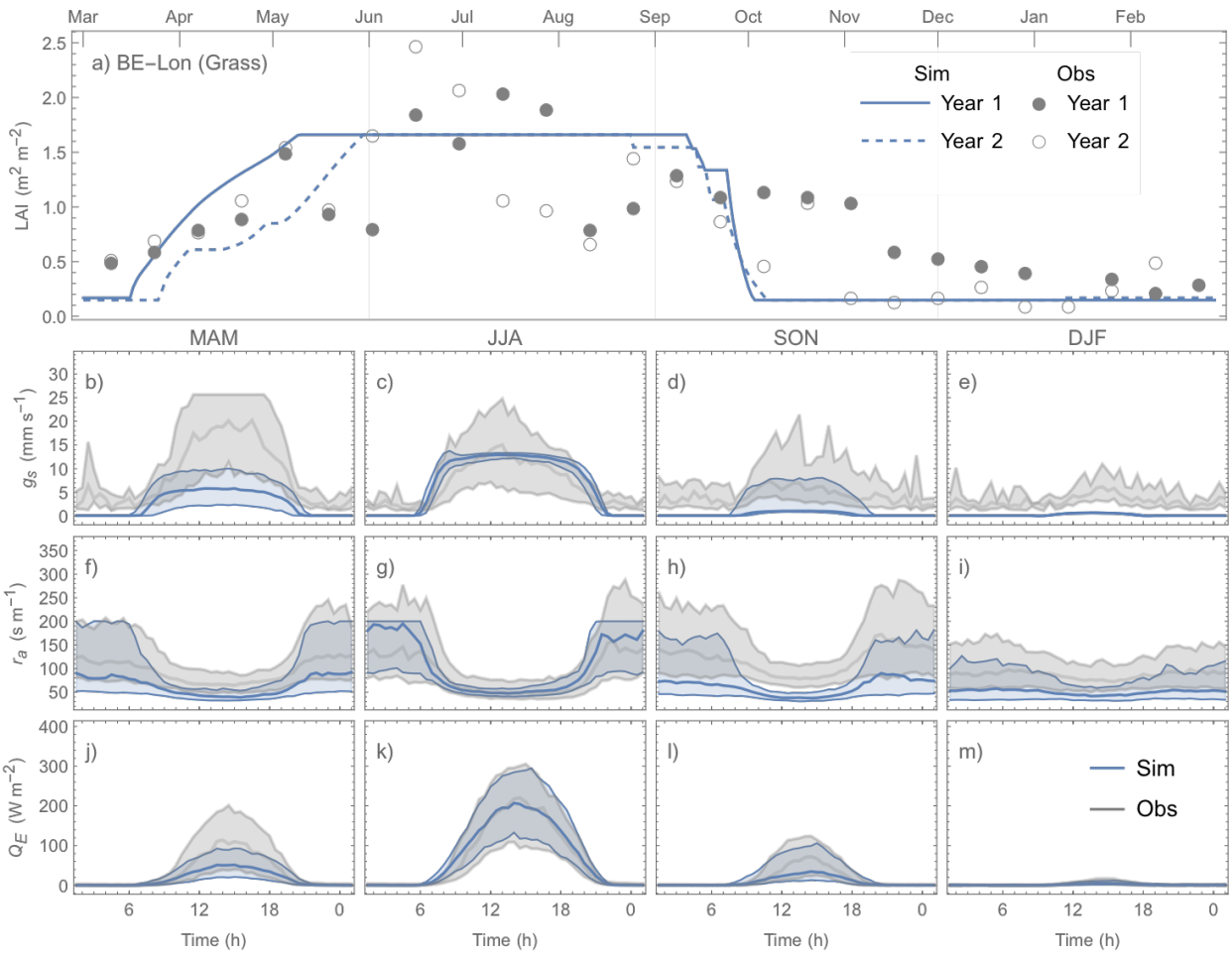

Figure 23 *As Fig. 19, but for BE-Lon (Grass, PS=0.88).*

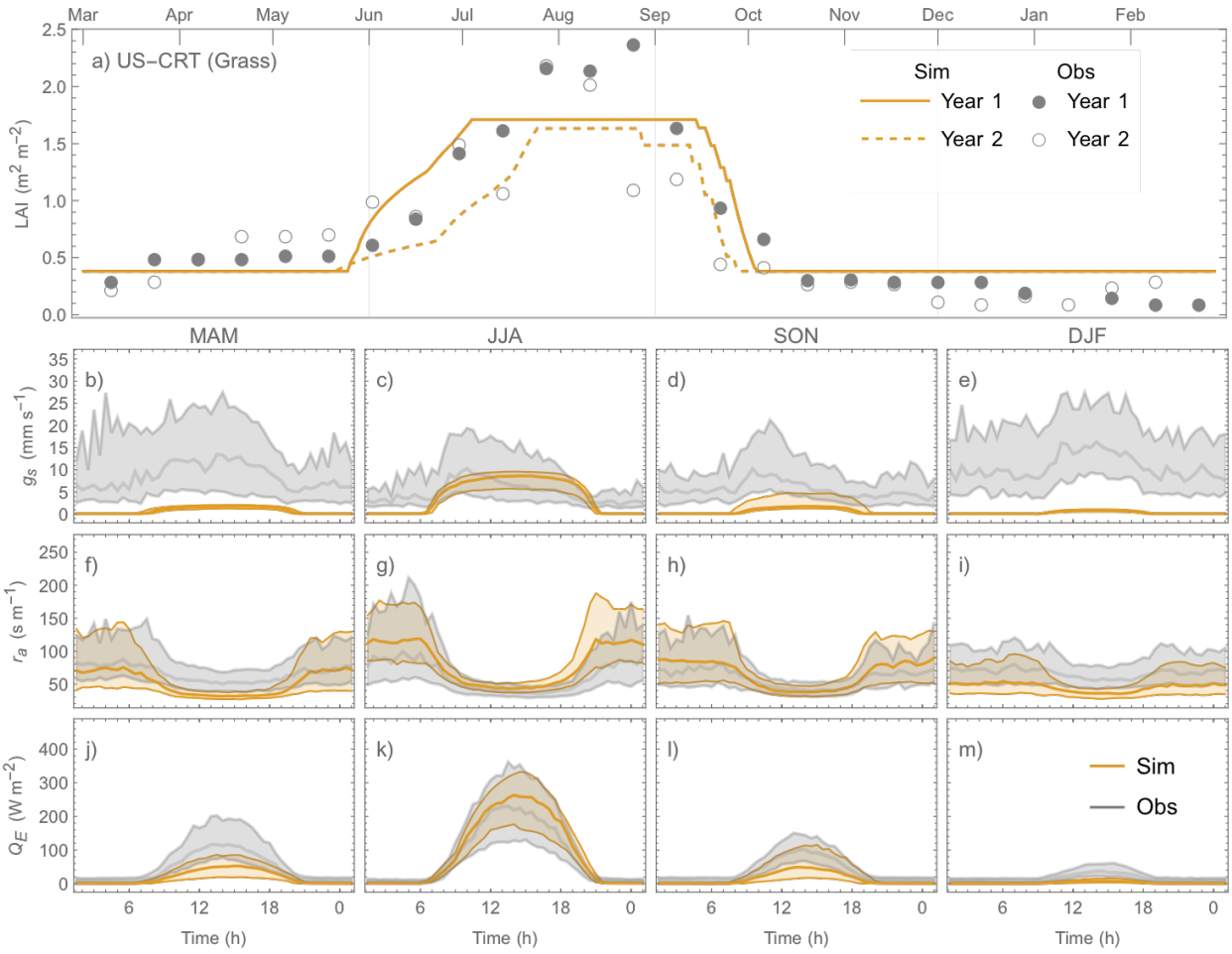

Figure 24 *As Fig. 19, but for US-CRT (Grass, PS=0.04).*

6 Concluding remarks

In this work, we derive parameters for SUEWS for fully vegetated land covers that are commonly found in background ('rural') contexts of cities, where SUEWS has been widely used to model urban climates. To facilitate derivation of SUEWS parameters we provide workflows in Jupyter notebooks (Sun et al. 2021) for leaf area index (LAI), albedo, Objective Hysteresis Model (OHM) coefficients, aerodynamic roughness parameters and surface conductance (g_s). We use these to determine parameters at 38 vegetated FLUXNET sites in North America, Europe and Australia. Using the derived parameters, we assess performance of SUEWS in predicting latent heat flux (Q_E) at different temporal scales (monthly and hourly).

It is concluded that:

- Where observations are available, we recommend determining local parameters, as derived parameters vary within PFT (Appendix C). The tools provided here are designed to facilitate this (Sect. 4).
- Given the global availability of MODIS LAI and reanalysis-based air temperature datasets (e.g., ERA5), it is feasible to derive site by site LAI parameters for SUEWS (Sect. 4.1).
- OHM coefficients for modelling storage heat flux derived here show clear seasonality: summertime (i.e., days warmer than annual median air temperature) a_1 and a_3 are smaller than their wintertime counterparts while the seasonal contrast in a_2 is smaller, suggesting seasonally varying values should be used for long-term (i.e. > one year) simulations.
- Surface conductance related parameters derived using summertime upper-boundary-based approach (Matsumoto et al. 2008), produce parameter related to solar radiation (G_K) and optimal air temperature (G_T) with some dependence on geographical locations, which could be used as a proxy to derive these two parameters.
- SUEWS modelled Q_E is particularly sensitive to surface conductance as informed by the attribution analysis using an analytical framework by McCuen (1974) and consistent with results of Beven (1975) that surface conductance plays a dominant role in moderating the bias in modelled Q_E.
- SUEWS configured with NOAH-based parameters has comparable prediction skill in Q_E compared to site-specific parameters when assessed by hit rate (HR) with medians being ~0.65. However, site-specific parameters improve SUEWS performance as shown by the mean absolute error (MAE) and mean bias error (MBE) metrics, becoming increasingly evident at finer temporal scales (monthly and hourly).
- SUEWS with site-specific parameters outperforms in cooler periods (i.e., winter and night) compared to warmer periods (i.e., summer and day): HR is consistently higher in the former periods than the latter (0.71 cf. 0.52 in median) while MAE (cooler vs. warmer seasons median: ~12 cf. ~31 W m^{-2}).
- Correctly predicting LAI timing dynamics has a crucial influence on overall Q_E model performance, followed by surface conductance g_s that is generally underestimated during cooler periods (more pronounced at night by ~3 mm s^{-1}).

As the first comprehensive study of SUEWS at multiple vegetated sites, we also identify future development and application needs:

- None of the simple LAI schemes in SUEWS account for hydrological impacts on LAI. Vegetation with shallow roots (e.g. US-SRG in Arizona, US, categorised as GRA according to IGBP, Fig. D2) are not well modelled when air temperature if the only phenology forcing variable. Hydrological feedback should be considered in future development of the LAI scheme in SUEWS.

- The specific humidity deficit surface conductance parameter relation needs improvement as a plateau-like trend is observed near the lower end (e.g., Fig. 9c).

- A potential source of parameters values for PFT beyond those studied here (i.e. values provided Appendix C, Sun et al. 2021) could be NOAH-based parameters (Appendix A) but these should be used with caution, as demonstrated (Section 5).

- More careful treatment of snow cover should be incorporated to enhance SUEWS capacity in high-latitude regions

Appendix A: NOAH-based equivalent values for surface conductance related parameters for SUEWS

The NOAH land surface scheme (Chen et al. 1996) uses a similar Jarvis-type parameterisation of surface conductance g_s as in SUEWS (i.e. Eqn. 13) but with different formulation of g_s sub-components from SUEWS (Eqn A1-A4 cf. Eqn. 15–18). The NOAH equations, using our notation are:

- Incoming solar radiation ($K_{\downarrow}$):

$$g_{NOAH}(K_{\downarrow}) = \frac{\frac{R_{\mathrm{cmin}}}{5000} + f}{1 + f} \tag{A1}$$

where $f = 0.55 \frac{K_{\downarrow}}{R_{\mathrm{gl}}} \frac{2}{\mathrm{LAI}}$ with R_{gl} an adjustable parameter for $K_{\downarrow}$.

- Air specific humidity (q):

$$g_{NOAH}(q) = \frac{1}{1 + h_s(q_s - q)} \tag{A2}$$

where h_s is the adjustable parameter for specific humidity q and q_s the saturation specific humidity.

- Air temperature (T_a):

$$g_{NOAH}(T_a) = 1 - 0.0016\left(T_{ref} - T_a\right)^2 \tag{A3}$$

where T_{ref} is the adjustable parameter for air temperature T_a.

- Soil moisture (θ_{soil}):

$$g_{NOAH}(\theta_{soil}) = \frac{\theta_{soil} - \theta_{WP}}{\theta_{FC} - \theta_{WP}} \tag{A4}$$

where θ_{FC} and θ_{WP} are field capacity and wilting point (see Table A2 for values of different soil types).

To use the NOAH parameters (as given in Table 1 and 2 of Chen and Duhdia 2001), we convert the NOAH parameters (Eqn. A1- A4) to the SUEWS required parameters (i.e. for Eqn. 15-18). The resulting SUEWS parameters (Table A1) are used (Sect. 5) to produce results in Fig. 14 and 15 denoted by NOAH.

Table A1 *NOAH-derived (data: based on Table 1 and 2 of Chen and Duhdia 2001) surface conductance related parameters for SUEWS*

	g_{max} [mm s^{-1}]	G_K [W m^{-2}]	G_T [°C]	T_L [°C]	T_H [°C]	$G_{q,base}$ [-]	$G_{q,shape}$ [-]	G_θ [-]
EBF	10.0	67	24.85	-0.15	49.85	0.361	0.932	0.002
DBF	10.0	67	24.85	-0.15	49.85	0.348	0.924	0.002
MF	10.0	66	24.85	-0.15	49.85	0.352	0.927	0.002
ENF	6.7	65	24.85	-0.15	49.85	0.361	0.932	0.002
GRA	25.0	336	24.85	-0.15	49.85	0.384	0.945	0.002
CSH	3.3	291	24.85	-0.15	49.85	0.372	0.938	0.002
OSH	2.5	275	24.85	-0.15	49.85	0.372	0.938	0.002
SAV	6.7	316	24.85	-0.15	49.85	0.372	0.938	0.002
CRO	25.0	336	24.85	-0.15	49.85	0.384	0.945	0.002
WET	6.7	316	24.85	-0.15	49.85	0.338	0.919	0.002
WSA	6.7	316	24.85	-0.15	49.85	0.372	0.938	0.002

Table A2 *Soil field capacity (θ_{FC}) and wilting point (θ_{WP}) used in NOAH (data: based on Table 2 of Chen and Duhdia 2001).*

	θ_{FC} [m^3 m^{-3}]	θ_{WP} [m^3 m^{-3}]
Sand	0.236	0.01
Loamy sand	0.283	0.028
Sandy loam	0.312	0.047
Silt loam	0.36	0.084
Silt	0.36	0.084
Loam	0.329	0.066
Sandy clay loam	0.314	0.067
Silty clay loam	0.387	0.12
Clay loam	0.382	0.103
Sandy clay	0.338	0.1
Silty clay	0.404	0.126
Clay	0.412	0.138

Except for the g_s function for air temperature – SUEWS and NOAH adopt the effectively same formulation – other g_s functions may produce different results even using the converted parameter values (Table A1). In particular, the shortwave radiation and specific humidity (Fig. A1), the SUEWS values (blue) are higher for all PFT types than NOAH (red). The role of soil type (Table A2) on the soil moisture deficit function (Fig. A2) results in larger differences at dry and mid-wet extremes.

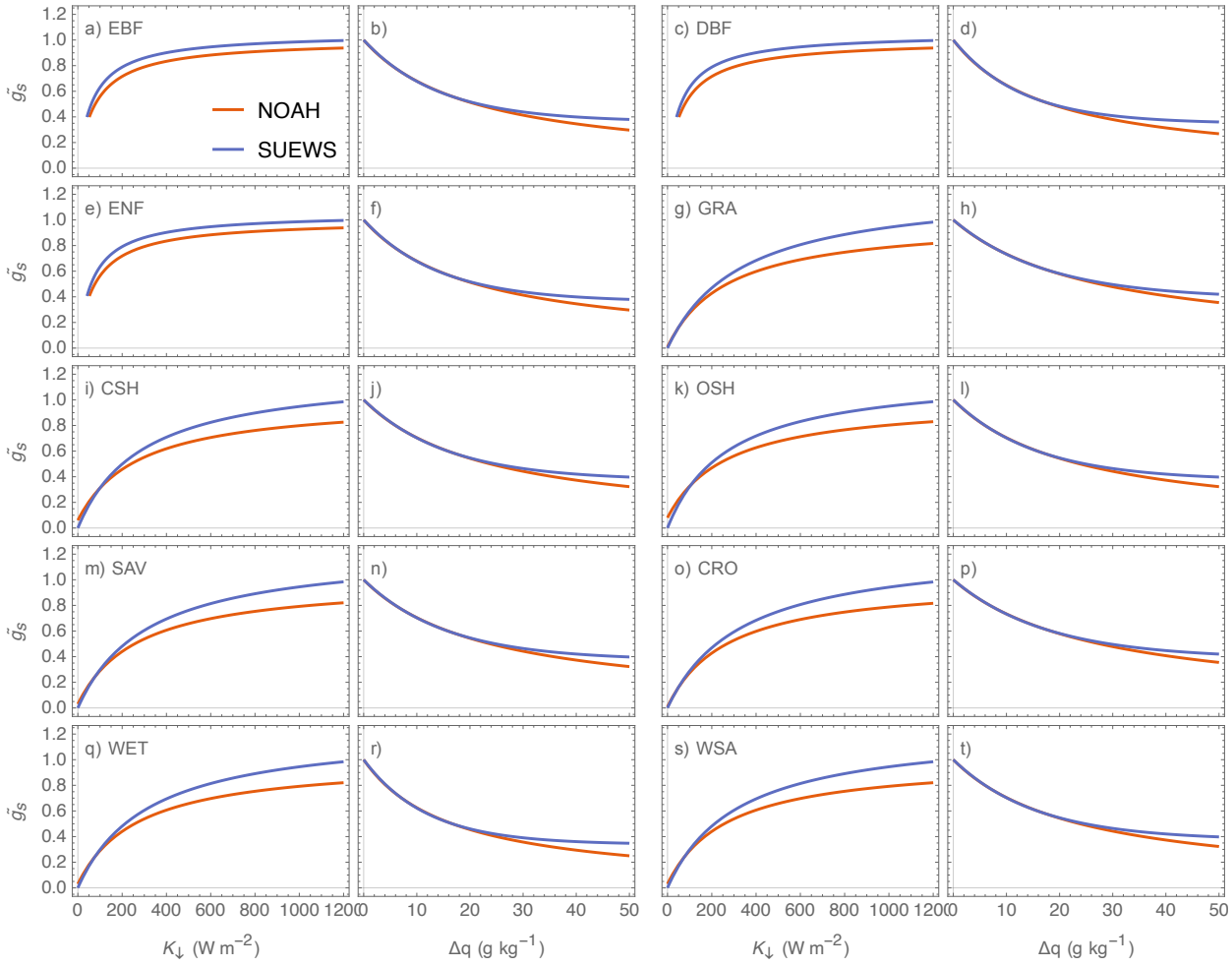

Figure A1 *NOAH (red) and SUEWS (blue) surface conductance functions for incoming solar radiation ($K_\downarrow$) and specific humidity deficit (Δq) for different IGBP PFTs.*

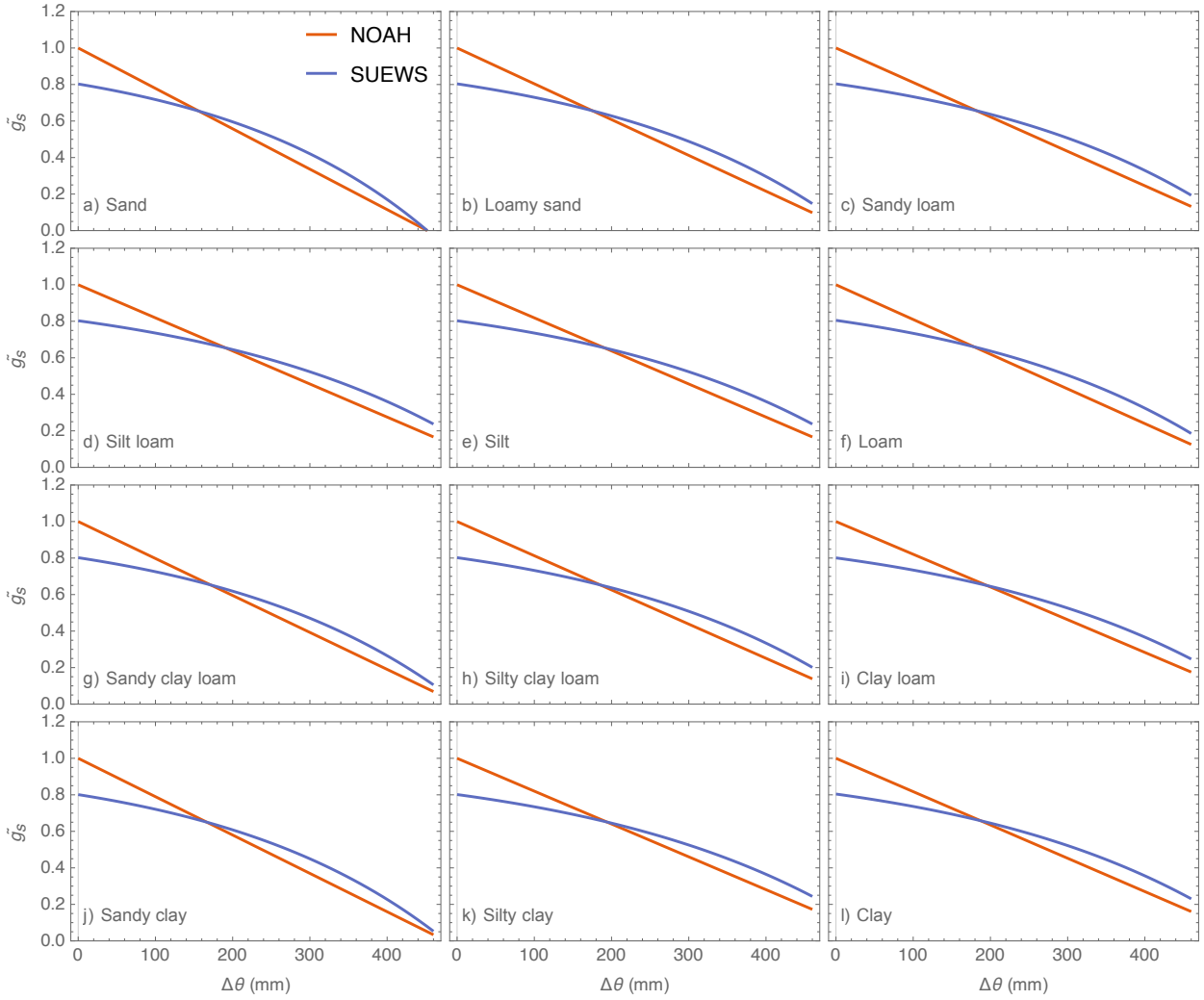

Figure A2. *As Fig A1 but for soil moisture deficit (Δθ) for different soil types with an assumed soil depth of 2000 mm. Soil hydraulic properties (field capacity θ_{FC} and wilting point θ_{WP}) are provided in Table A2.*

Appendix B: Derivation of roughness length and zero-plane displacement height for momentum

The aerodynamic roughness parameters for momentum (roughness length z_{0m} and zero-plane displacement height z_d) are derived using observed u_* and u under neutral conditions (i.e. $\left|\frac{z_m - z_d}{L}\right| < 0.01$ with an initial estimate of $z_d = 0.7H_c$) of different vegetation stages based on LAI (see Sect. 4.1 for classification details) by the least-square method for the following relation (Monin and Obukhov, 1954):

$$u = \frac{u_*}{\kappa} \ln\left(\frac{z_m - z_d}{z_{0m}}\right) \tag{B1}$$

where κ is the von Kármán constant (0.4 is used here). In particular, for sites with varying canopy height H_c, z_{0m} and z_d are derived for each of the periods when H_c stayed unchanged and more than 20 observational pairs of u_* and u are available.

Using the derived z_{0m} and z_d, f_0 and f_d parameters can be obtained (Eqn. 9 and 10). These is considerable intra-PFT variability of both f_0 and f_d (Fig. B1). There are also intra-site variations associated with varying H_c. Given the large variability in both f_0 and f_d, the rule-of-thumb approach would incur large bias in estimated aerodynamic and surface resistances and subsequently the modelled Q_E. To reduce such bias, in the evaluation of the other sub-models and parameter determinations in this paper, we use the derive z_{0m} and z_d determined for each vegetation stage and site.

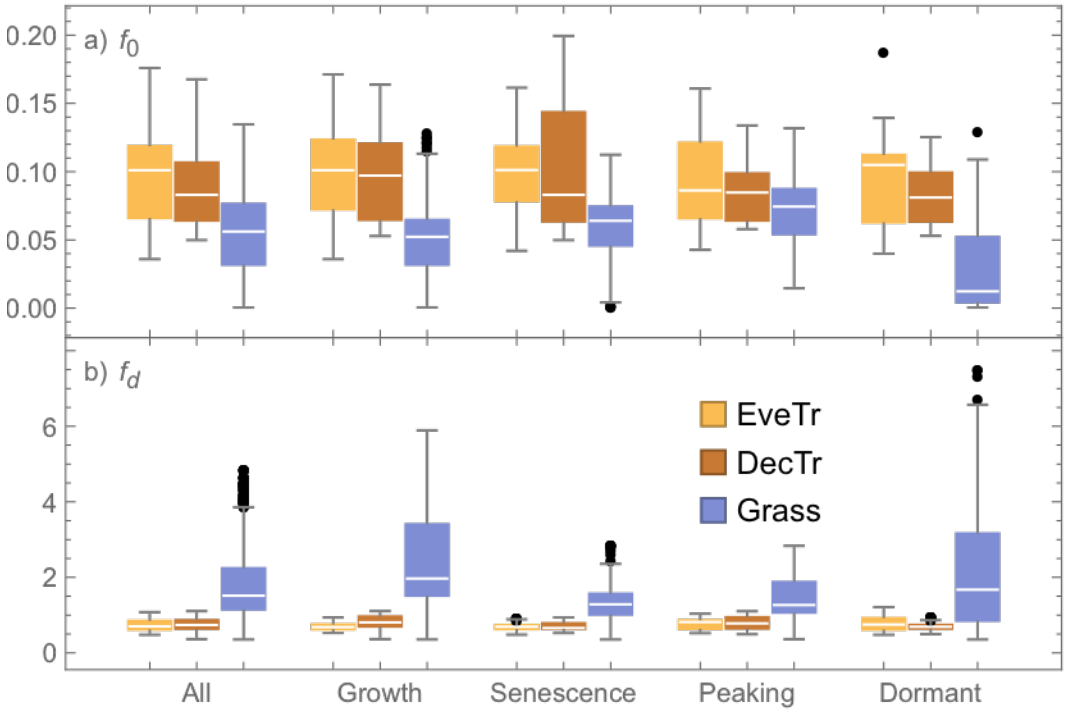

***Figure B1**. Relations between canopy height (H_c) and a) roughness length for momentum (z_{0m}, Eqn. B2) and b) displacement height (z_d, Eqn. B3) for different vegetation stages based on LAI (see Sect. 4.1 for classification details)*

Modelled wind speed under neutral conditions matches well with observations at 38 study sites with MAE < 0.3 m s^{-1} and MBE close to zero (Fig. B2). Of the three SUEWS PFTs, 'Grass' sites have the poorer performance. This is probably because this PFT includes crops which will change frequently because of crop rotations: cereal, potato, sugar beet at BE-Lon (Moureaux et al., 2006); winter barley, rapeseed, winter wheat, maize and spring barley at DE-Kli (Prescher et al., 2010), maize and soybean at US-Ne2 and US-Ne3).

Figure B2 *MAE (blue) and MBE (orange) for modelled wind speed under neutral conditions for three SUEWS PFTs: a) EveTr, b) DecTr and c) Grass.*

Appendix C: SUEWS parameters derived at selected FLUXNET sites

Table C1 *LAI and albedo related parameters at 38 sites (Table 3 gives site information) derived using FLUXNET2015 dataset (Sect. 4.1).*

	α_{min} [-]	α_{max} [-]	LAI_{max} [m^2 m^{-2}]	LAI_{min} [m^2 m^{-2}]	GDD_{full} [°C day]	SDD_{full} [°C day]	$T_{base,GDD}$ [°C]	$T_{base,SDD}$ [°C]	$\omega_{1,GDD}$ [-]	$\omega_{1,SDD}$ [-]	$\omega_{2,GDD}$ [-]	$\omega_{2,SDD}$ [-]
AT-Neu	0.23	0.19	2.24	0.18	1200.58	-1015.40	-0.20	14.02	-2.00	-3.02E-03	5.35E-05	0.09
AU-ASM	0.12	0.09	0.30	0.20	93.17	-31.48	13.90	16.42	-1.32	-2.21E-03	1.43E-05	0.97
AU-DaS	0.14	0.12	1.86	0.97	350.98	-78.63	25.74	24.90	-2.00	-5.45E-03	5.29E-05	1.37
AU-Gin	0.13	0.11	1.09	0.60	239.14	-96.09	12.73	17.21	-2.00	-1.16E-03	7.87E-05	2.95
AU-Wom	0.10	0.09	4.51	1.19	404.14	-43.42	5.50	7.86	-2.00	-5.17E-03	2.10E-03	1.17
BE-Lon	0.17	0.14	1.66	0.15	264.31	-467.14	8.63	14.53	-2.00	-2.27E-03	4.64E-04	3.33
CA-Gro	0.09	0.08	2.97	0.65	1000.69	-300.71	-0.62	13.37	-2.00	-5.50E-04	2.88E-04	1.72
CA-Oas	0.12	0.11	3.87	0.56	252.15	-193.36	8.69	13.81	-1.71	-3.22E-03	3.81E-03	1.65
CA-Qfo	0.11	0.06	1.82	0.20	932.53	-675.56	-4.41	12.84	-1.26	-1.05E-03	6.79E-05	0.57
CA-SF2	0.12	0.11	2.74	0.50	781.58	-382.78	1.43	12.35	-2.00	-9.12E-04	2.08E-04	3.03
CA-SF3	0.10	0.09	2.22	0.45	724.36	-598.25	1.40	14.45	-2.00	-7.55E-03	1.24E-04	0.10
CA-TP4	0.09	0.08	2.57	0.43	1042.85	-599.76	4.54	18.51	-2.00	-3.77E-03	1.32E-04	0.14
CH-Cha	0.21	0.18	2.39	0.52	161.91	-369.59	2.69	9.41	-2.00	-6.79E-03	2.45E-03	1.04
CH-Dav	0.07	0.06	2.04	0.20	645.94	-380.00	1.95	9.97	-1.36	-3.69E-04	1.14E-04	2.83
CH-Oe1	0.22	0.18	1.98	0.31	399.90	-486.85	2.78	12.45	-2.00	-1.39E-03	4.58E-04	0.29
DE-Gri	0.21	0.19	2.52	0.69	369.12	-383.65	3.10	12.72	-2.00	-7.57E-03	6.59E-04	0.05
DE-Hai	0.13	0.09	3.82	0.98	101.43	-49.58	7.46	9.89	-0.09	-1.00E-02	3.49E-03	4.00
DE-Kli	0.19	0.14	2.24	0.30	371.62	-129.27	2.81	9.29	-2.00	-7.34E-03	4.20E-04	1.46
DE-Lkb	0.22	0.14	2.68	0.51	967.50	-293.93	-1.32	7.59	-2.00	-3.45E-03	1.45E-04	0.52
DE-Obe	0.07	0.06	2.84	0.59	349.45	-306.51	1.77	7.74	-2.00	-7.57E-03	1.05E-03	1.27

FI-Hyy	0.10	0.09	2.73	0.43	859.30	-512.51	0.08	14.97	-2.00	-3.98E-03	3.35E-04	0.10
FR-LBr	0.11	0.10	2.35	0.62	322.30	-263.61	11.58	17.10	-2.00	-2.58E-03	7.28E-04	2.51
IT-Col	0.13	0.11	3.12	0.54	390.41	-424.85	3.60	11.45	-2.00	-7.40E-04	1.22E-03	0.85
IT-SRo	0.09	0.07	2.73	0.92	481.73	-564.19	8.39	18.06	-2.00	-2.68E-03	6.75E-04	0.07
IT-Tor	0.23	0.18	2.08	0.20	625.92	-467.45	0.70	9.16	-2.00	-9.33E-04	1.58E-04	1.45
NL-Loo	0.10	0.09	2.01	0.49	676.48	-937.96	6.27	16.31	-2.00	-6.60E-03	9.67E-05	0.02
US-AR1	0.15	0.14	0.96	0.27	387.82	-929.25	10.88	22.53	-2.00	-2.31E-03	3.71E-05	0.06
US-CRT	0.12	0.11	2.53	0.38	23.74	-264.69	25.24	17.99	-2.00	-1.21E-03	4.49E-03	1.25
US-Goo	0.20	0.16	3.13	0.73	131.20	-276.51	16.85	19.13	-2.00	-5.99E-04	7.11E-03	2.09
US-IB2	0.15	0.13	1.94	0.21	1403.13	-940.31	1.12	19.90	-1.74	-7.04E-03	4.08E-05	0.06
US-Me6	0.15	0.11	1.46	0.61	22.89	-309.48	6.70	4.74	-2.00	-5.80E-04	2.91E-03	0.15
US-MMS	0.12	0.11	5.00	1.01	68.61	-50.83	13.97	15.79	-0.45	-7.11E-03	8.30E-03	2.22
US-Ne1	0.16	0.14	2.13	0.34	475.09	-321.98	14.84	22.34	-1.80	-7.23E-04	2.07E-04	1.62
US-Ne2	0.16	0.13	2.08	0.30	469.13	-380.78	14.65	22.42	-1.83	-2.03E-03	2.13E-04	0.41
US-Ne3	0.17	0.16	2.18	0.33	491.72	-317.46	14.89	22.64	-1.60	-5.25E-04	2.15E-04	1.47
US-NR1	0.14	0.14	1.53	0.51	640.96	-1239.29	-0.32	11.62	-2.00	-1.20E-03	9.67E-05	0.04
US-Oho	0.14	0.12	2.78	0.45	1540.19	-981.83	1.50	21.71	-1.65	-5.24E-03	9.67E-05	0.05
US-Syv	0.16	0.10	4.81	0.66	461.96	-202.37	4.30	15.08	-1.67	-3.25E-03	2.33E-03	1.12

818 ***Table C2*** *As Table C1 but for OHM related parameters (Sect. 4.2)*

	a_1 [-]		a_2 [h]		a_3 [W m^{-2}]	
	summer	**winter**	**summer**	**winter**	**summer**	**winter**
AT-Neu	0.37	0.88	0.05	0.02	-12.12	11.15
AU-ASM	0.39	0.39	0.15	0.13	-26.44	-35.45
AU-DaS	0.31	0.30	0.05	0.06	-29.17	-21.82
AU-Gin	0.40	0.25	0.17	0.21	-11.35	-25.75
AU-Wom	0.29	0.29	0.10	0.08	3.54	-18.13
BE-Lon	0.32	0.82	0.18	0.04	-3.58	8.00
CA-Gro	0.31	0.51	0.15	0.19	-9.62	-8.94
CA-Oas	0.27	0.45	0.13	0.25	-6.84	-0.58
CA-Qfo	0.30	0.43	0.22	0.25	-10.70	-1.50
CA-SF2	0.16	0.46	0.15	0.09	-17.05	-3.39
CA-SF3	0.25	0.60	0.20	0.09	-22.22	-8.67
CA-TP4	0.28	0.42	0.17	0.13	-7.94	1.07
CH-Cha	0.25	0.67	0.05	0.00	-29.09	-8.37
CH-Dav	0.56	0.65	0.13	0.11	-29.23	-12.08
CH-0e1	0.34	0.67	0.08	0.12	-22.53	-6.21
DE-Gr1	0.44	0.76	0.04	0.02	-6.13	5.14
DE-Hai	0.15	0.21	-0.01	0.15	-1.31	9.81
DE-Kli	0.45	0.77	0.12	0.07	-11.62	4.91
DE-Lkb	0.23	0.84	0.09	-0.04	-31.59	-18.49
DE-0be	0.33	0.53	-0.06	0.02	-10.33	-8.95
Fl-Hyy	0.23	0.68	0.17	0.09	-8.75	7.89
FR-LBr	0.27	0.43	0.19	0.17	-17.30	-8.04
IT-C01	0.36	0.43	0.14	0.22	-4.56	-10.00
IT-SRo	0.31	0.51	0.27	0.15	-5.40	13.57
IT-Tor	0.23	0.94	0.09	0.05	-18.92	4.31
NL-Loo	0.24	0.44	0.14	0.20	1.06	2.90
US-ARI	0.18	0.17	0.16	0.11	-26.72	-16.50
US-CRT	0.32	0.63	0.11	0.06	-11.14	-6.23
US-Goo	0.38	0.41	0.04	0.07	-16.06	-20.52
US-lB2	0.29	0.37	0.00	0.03	-4.97	-6.43
US-Me6	0.35	0.51	0.21	0.12	-24.00	-0.93
US-MMS	0.34	0.45	0.19	0.25	-7.46	-7.21
US-Ne1	0.30	0.56	0.09	0.03	-13.72	-9.05
US-Ne2	0.29	0.51	0.06	0.04	-14.54	-9.19
US-Ne3	0.29	0.55	0.04	-0.02	-17.87	-8.34
US-NRI	0.27	0.22	0.05	0.06	-7.97	-15.95
US-Oho	0.32	0.44	0.10	0.16	-13.31	-12.73
US-syv	0.33	0.33	0.06	0.13	-9.21	-0.93

819 ***Table C3*** *As Table C1, but for surface conductance related parameters (Sect. 4.3)*

	g_{max} [mm s^{-1}]	G_K [W m^{-2}]	G_T [°C]	T_L [°C]	T_H [°C]	$G_{q,base}$ [-]	$G_{q,shape}$ [-]	G_θ [-]	$\Delta\theta_{WP}$ [mm]

AT-Neu	39.6193	50.00	23.67	-15.74	31.59	0.50	0.90	0.04	687.75
AU-ASM	15.73	288.38	26.77	8.00	34.39	0.40	0.90	0.01	409.50
AU-DaS	19.92	83.22	37.78	-30.00	38.00	0.50	0.90	0.02	414.75
AU-Gin	7.44	94.79	13.23	-14.59	41.54	0.41	0.90	0.06	446.25
AU-Wom	30.63	70.26	14.73	2.00	41.91	0.36	0.90	0.10	535.50
BE-Lon	25.64	74.21	23.22	5.31	36.41	0.50	0.90	0.01	430.50
CA-Gro	22.96	50.00	5.33	-30.00	36.00	0.40	0.90	0.01	876.75
CA-Oas	26.76	50.00	14.53	-30.00	30.89	0.50	0.90	0.01	603.75
CA-Qfo	15.56	50.00	11.62	-0.93	46.81	0.22	0.90	0.01	404.25
CA-SF2	23.59	91.88	12.21	-29.99	33.65	0.50	0.90	0.03	525.00
CA-SF3	23.95	50.00	-0.01	-30.00	38.43	0.36	0.90	0.07	514.50
CA-TP4	23.10	50.00	19.12	-9.57	50.00	0.50	0.90	0.03	446.25
CH-Cha	46.30	126.77	35.86	-30.00	50.00	0.50	0.90	0.10	173.25
CH-Dav	18.14	50.00	4.55	-15.93	49.96	0.50	0.90	0.07	141.75
CH-Oe1	41.74	77.78	16.52	-0.99	50.00	0.50	0.90	0.01	556.50
DE-Gri	25.43	142.40	20.71	-23.20	36.09	0.50	0.90	0.00	750.75
DE-Hai	22.45	69.16	5.61	-29.82	34.65	0.27	0.90	0.01	514.50
DE-Kli	24.50	51.37	19.63	-30.00	26.26	0.50	0.90	0.01	824.25
DE-Lkb	32.34	85.39	-0.12	-30.00	50.00	0.50	0.90	0.02	278.25
DE-Obe	14.76	50.01	4.44	-28.20	34.78	0.41	0.90	0.03	283.50
Fl-Hyy	17.23	64.75	18.94	4.00	34.44	0.40	0.90	0.01	708.75
FR-LBr	24.48	50.00	14.03	-8.96	33.12	0.33	0.90	0.01	1065.75
IT-Col	14.66	50.00	13.96	-12.26	50.00	0.50	0.90	0.02	425.25
IT-SRo	20.57	50.00	7.66	-30.00	49.99	0.47	0.90	0.01	971.25
IT-Tor	42.23	73.54	23.20	-15.96	49.99	0.50	0.90	0.09	294.00
NL-Loo	16.53	50.00	17.70	6.00	37.06	0.35	0.90	0.10	252.00
US-AR1	27.51	181.15	16.31	6.00	34.00	0.03	0.90	0.01	315.00
US-CRT	27.43	50.00	30.54	-14.00	42.02	0.50	0.90	0.10	824.25
US-Goo	41.46	172.08	24.45	-10.87	50.00	0.50	0.90	0.03	404.25
US-IB2	48.78	50.00	29.19	-7.90	36.00	0.50	0.90	0.06	483.00
US-Me6	13.70	92.88	3.44	-10.00	42.71	0.11	0.90	0.01	525.00
US-MMS	22.54	182.23	27.06	-0.24	36.62	0.50	0.90	0.01	845.25
US-Ne1	52.14	50.00	29.84	-30.00	34.43	0.50	0.90	0.04	519.75
US-Ne2	53.45	59.97	32.04	-30.00	34.02	0.50	0.90	0.10	383.25
US-Ne3	44.55	53.41	30.84	-30.00	50.00	0.50	0.90	0.07	645.75
US-NRI	15.91	52.94	5.51	-11.90	33.80	0.43	0.90	0.02	509.25
US-Oho	40.01	56.33	31.08	-29.99	36.53	0.50	0.90	0.10	220.50
US-Syv	16.85	130.28	18.77	-4.00	40.65	0.50	0.90	0.01	456.75

820

Appendix D: Typical Intra-annual LAI dynamics under contrasting meteorological controls

Given sufficient CO_2, vegetation phenology indicated by LAI dynamics, is predominantly controlled by input energy and water (Fang et al. 2019). Two variables that capture this seasonal variability are air temperature and precipitation. Different intra-annual LAI dynamics are evident between sites, with contrasting meteorological controls:

a) Thermally dominant (US-MMS; Fig. D1): Intra-annual cumulative precipitation at US-MMS steadily increases throughout the year (Fig. D1a), implying a fairly even distribution of water supply; while air temperature gradually increases from the mid winter (beginning of a year), peaks in August and decrease with the start of the next winter (Fig. D1b). The LAI pattern at US-MMS responds to the air temperature, notably the growing degrees days (GDD) and then autumn senescence (SDD). This inverse "U"-shape typifies sites with thermally-dominant LAI dynamics. These types of sites are well parameterised by the current LAI scheme in SUEWS (Sect. 2.2.1).

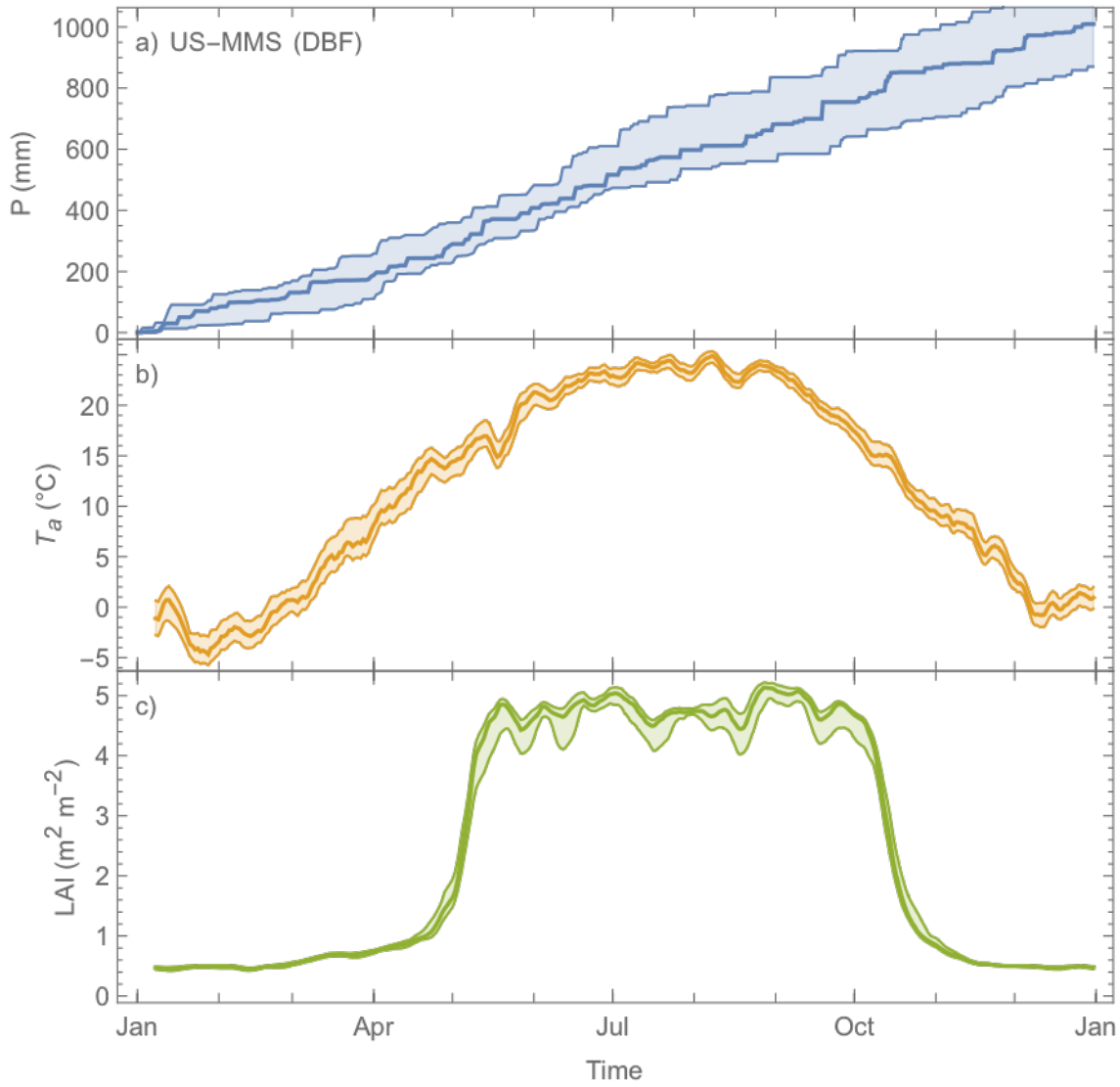

Figure D1 *Median (line) and interquartile range (shading) daily variation at US-MMS a DBF site during the period 2002–2015 of (a) precipitation (cumulative), (b) air temperature (7-day moving average) and (c) LAI (7-day moving average).*

b) Rainfall and thermal controls (US-SRG; Fig. D2): at this grassland site in Arizona, US the intra-annual precipitation has clear dry and wet seasons. The monsoon wet season after the peak air temperature in July through September (Fig. D2a), which has warmest air temperatures, Unlike US-MMS (Fig. D2b), the peak air temperature is more distinct (for a shorter period). A clear relation between the onset of rainfall and LAI enhancement can be seen but the GDD and SDD relation differs from US-MMS and it not captured by the current models in SUEWS. The rainfall and enhanced LAI and Q_E are associated with cooler daily air temperatures. Sites where the LAI dynamics are not captured are not explored further in this paper.

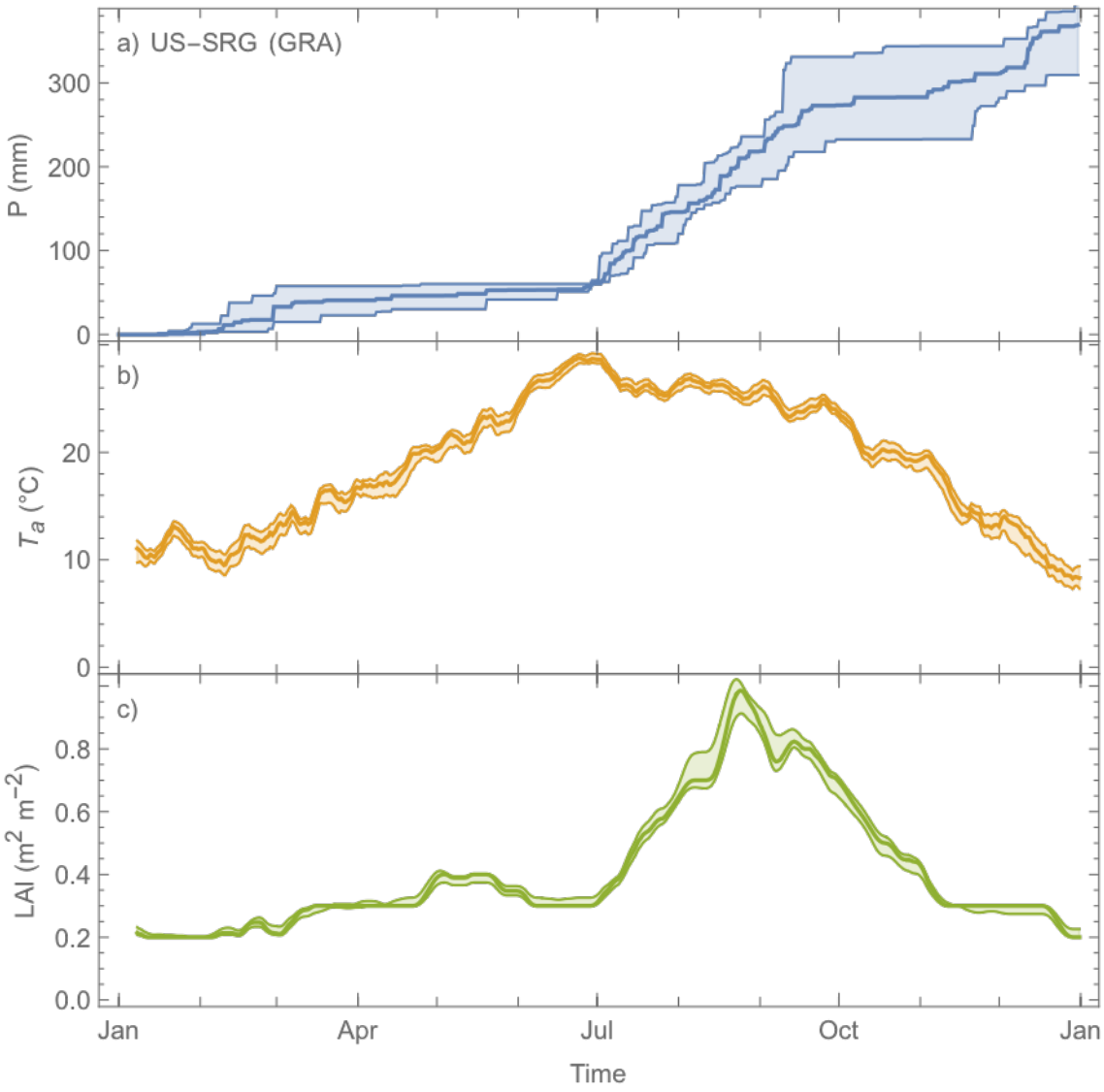

Figure D2 *As Fig. D1, but for US-SRG (GRA according to IGBP; time span: 2008–2015; DOI: 10.18140/FLX/1440114)*

Code and data availability

All source codes, input and output data are archived at Zenodo in Sun et al. (2021).

Author contribution

HO, TS and SG contributed to data preparation, parameter derivation, running simulations and writing the paper. HO led the initial and TS the revised versions of this work. All other authors (DB, AB, JC, ZD, HI,

and JM) provided data for analysis of this work at different stages (some not used in this paper), interpreted the results, and reviewed the manuscript.

Competing interest

The authors declare that they have no conflict of interest.

Acknowledgments

This work is funded by NERC-COSMA project (NE/S005889/1), Newton Fund Met Office CSSP-China (SG), NERC Independent Research Fellowship (NE/P018637/1), and National Natural Science Foundation of China (41875013; Zhiqiu Gao and Zexia Duan).

References

Anandakumar, K.: A study on the partition of net radiation into heat fluxes on a dry asphalt surface, Atmos Environ, 33(24–25), 3911 3918, doi:10.1016/s1352-2310(99)00133-8, 1999.

André, J.-C., Goutorbe, J.-P. and Perrier, A.: HAPEX–MOBLIHY: A Hydrologic Atmospheric Experiment for the Study of Water Budget and Evaporation Flux at the Climatic Scale, B Am Meteorol Soc, 67(2), 138–144, doi:10.1175/1520-0477(1986)067<0138:hahaef>2.0.co;2, 1986.

Ao, X., Grimmond, C. S. B., Ward, H. C., Gabey, A. M., Tan, J., Yang, X.-Q., Liu, D., Zhi, X., Liu, H. and Zhang, N.: Evaluation of the Surface Urban Energy and Water Balance Scheme (SUEWS) at a Dense Urban Site in Shanghai: Sensitivity to Anthropogenic Heat and Irrigation, J. Hydrometeorol., 19(12), 1983–2005, doi:10.1175/JHM-D-18-0057.1, 2018.

Asaadi, A., Arora, V. K., Melton, J. R. and Bartlett, P.: An improved parameterization of leaf area index (LAI) seasonality in the Canadian Land Surface Scheme (CLASS) and Canadian Terrestrial Ecosystem Model (CTEM) modelling framework, Biogeosciences, 15(22), 6885–6907, doi:10.5194/bg-15-6885-2018, 2018.

Baldocchi, D., Falge, E., Gu, L., Olson, R., Hollinger, D., Running, S., Anthoni, P., Bernhofer, C., Davis, K., Evans, R., Fuentes, J., Goldstein, A., Katul, G., Law, B., Lee, X., Malhi, Y., Meyers, T., Munger, W., Oechel, W., Paw, U. K. T., Pilegaard, K., Schmid, H. P., Valentini, R., Verma, S., Vesala, T., Wilson, K. and Wofsy, S.: FLUXNET: A New Tool to Study the Temporal and Spatial Variability of Ecosystem-Scale Carbon Dioxide, Water Vapor, and Energy Flux Densities, Bull. Am. Meteorol. Soc., 82(11), 2415–2434, doi:10.1175/1520-0477(2001)082<2415:FANTTS>2.3.CO;2, 2001.

Balsamo, G., Beljaars, A., Scipal, K., Viterbo, P., Hurk, B. van den, Hirschi, M., and Betts, A. K.: A Revised Hydrology for the ECMWF Model: Verification from Field Site to Terrestrial Water Storage and Impact in the Integrated Forecast System, 10, 623–643, https://doi.org/10.1175/2008jhm1068.1, 2009.

Bauerle, W. L., Oren, R., Way, D. A., Qian, S. S., Stoy, P. C., Thornton, P. E., Bowden, J. D., Hoffman, F. M. and Reynolds, R. F.: Photoperiodic regulation of the seasonal pattern of photosynthetic capacity

and the implications for carbon cycling, Proc. Natl. Acad. Sci. U. S. A., 109(22), 8612–8617, doi:10.1073/pnas.1119131109, 2012.

Bergeron, O., Margolis, H. A., Black, T. A., Coursolle, C., Dunn, A. L., Barr, A. G. and Wofsy, S. C.: Comparison of carbon dioxide fluxes over three boreal black spruce forests in Canada, Glob. Chang. Biol., 13(1), 89–107, doi:10.1111/j.1365-2486.2006.01281.x, 2007.

Beven, K.: A sensitivity analysis of the Penman-Monteith actual evapotranspiration estimates, J Hydrol, 44(3–4), 169–190, doi:10.1016/0022-1694(79)90130-6, 1979.

Billesbach, D., Bradford, J. and Torn, M.: AmeriFlux US-AR1 ARM USDA UNL OSU Woodward Switchgrass 1, AmeriFlux Netw., doi:10.17190/AMF/1246137, 2009.

Bloomfield, P.: Fourier Analysis of Time Series: An Introduction. New York: Wiley-Interscience, 2000

Bobée, C., Ottlé, C., Maignan, F., De Noblet-Ducoudré, N., Maugis, P., Lézine, A. M. and Ndiaye, M.: Analysis of vegetation seasonality in Sahelian environments using MODIS LAI, in association with land cover and rainfall, J. Arid Environ., 84, 38–50, doi:10.1016/j.jaridenv.2012.03.005, 2012.

Bosveld, F. C. and Bouten, W.: Evaluation of transpiration models with observations over a Douglas-fir forest, Agr Forest Meteorol, 108(4), 247–264, doi:10.1016/s0168-1923(01)00251-9, 2001.

Brutsaert, W.: Evaporation into the Atmosphere, Springer Netherlands, Dordrecht., 1982.

Campbell, G. S. and Norman, J. M.: An Introduction to Environmental Biophysics, in An Introduction to Environmental Biophysics, pp. 1–13, Springer New York, New York, NY., 1998.

Cescatti, A., Marcolla, B., Vannan, S. K. S., Pan, J. Y., Román, M. O., Yang, X., Ciais, P., Cook, R. B., Law, B. E., Matteucci, G., Migliavacca, M., Moors, E., Richardson, A. D., Seufert, G. and Schaaf, C. B.: Intercomparison of MODIS albedo retrievals and in situ measurements across the global FLUXNET network, Remote Sens Environ, 121, 323–334, doi:10.1016/j.rse.2012.02.019, 2012.

Chen, F., Mitchell, K., Schaake, J., Xue, Y., Pan, H., Koren, V., Duan, Q. Y., Ek, M., and Betts, A.: Modeling of land surface evaporation by four schemes and comparison with FIFE observations, J Geophys Res Atmospheres, 101, 7251–7268, https://doi.org/10.1029/95jd02165, 1996.

Chen, F. and Dudhia, J.: Coupling an advanced land surface-hydrology model with the Penn State-NCAR MM5 modeling system. Part I: Model implementation and sensitivity, Mon Weather Rev, 129(4), 569 585, doi:10.1175/1520-0493(2001)129<0569:caalsh>2.0.co;2, 2001.

Chu, H., Luo, X., Ouyang, Z., Chan, W. S., Dengel, S., Biraud, S. C., Torn, M. S., Metzger, S., Kumar, J., Arain, M. A., Arkebauer, T. J., Baldocchi, D., Bernacchi, C., Billesbach, D., Black, T. A., Blanken, P. D., Bohrer, G., Bracho, R., Brown, S., Brunsell, N. A., Chen, J., Chen, X., Clark, K., Desai, A. R., Duman, T., Durden, D., Fares, S., Forbrich, I., Gamon, J. A., Gough, C. M., Griffis, T., Helbig, M., Hollinger, D., Humphreys, E., Ikawa, H., Iwata, H., Ju, Y., Knowles, J. F., Knox, S. H., Kobayashi, H., Kolb, T., Law, B., Lee, X., Litvak, M., Liu, H., Munger, J. W., Noormets, A., Novick, K., Oberbauer, S. F., Oechel, W., Oikawa, P., Papuga, S. A., Pendall, E., Prajapati, P., Prueger, J., Quinton, W. L., Richardson, A. D., Russell, E. S., Scott, R. L., Starr, G., Staebler, R., Stoy, P. C., Stuart-Haëntjens, E., Sonnentag, O., Sullivan, R. C., Suyker, A., Ueyama, M., Vargas, R., Wood, J. D., and Zona, D.: Representativeness of Eddy-Covariance flux footprints for areas surrounding AmeriFlux sites, Agricultural and Forest Meteorology, 301–302, 108350, doi:10.1016/j.agrformet.2021.108350, 2021.

926 Curtis, P. S., Hanson, P. J., Bolstad, P., Barford, C., Randolph, J. C., Schmid, H. P. and Wilson, K. B.:
927 Biometric and eddy-covariance based estimates of annual carbon storage in five eastern North American
928 deciduous forests, Agric. For. Meteorol., 113(1–4), 3–19, doi:10.1016/S0168-1923(02)00099-0, 2002.

929 Doll, D., Ching, J. K. S. and Kaneshiro, J.: Parameterization of subsurface heating for soil and concrete
930 using net radiation data, Boundary-Layer Meteorol., 32(4), 351–372, doi:10.1007/BF00122000, 1985.

931 Ek, M. B., Mitchell, K. E., Lin, Y., Rogers, E., Grunmann, P., Koren, V., Gayno, G. and Tarpley, J. D.:
932 Implementation of Noah land surface model advances in the National Centers for Environmental
933 Prediction operational mesoscale Eta model, J. Geophys. Res. Atmos., 108(D22), 2002JD003296,
934 doi:10.1029/2002JD003296, 2003.

935 Ershadi, A., McCabe, M. F., Evans, J. P., Chaney, N. W., and Wood, E. F.: Multi-site evaluation of
936 terrestrial evaporation models using FLUXNET data, Agr Forest Meteorol, 187, 46–61,
937 doi:10.1016/j.agrformet.2013.11.008, 2014.

938 Ester, M., Kriegel, H.-P., Sander, J., and Xu, X.: A density-based algorithm for discovering clusters in
939 large spatial databases with noise, in: Proceedings of the Second International Conference on Knowledge
940 Discovery and Data Mining, Portland, Oregon, 226–231, 1996.

941 Fang, H., Baret, F., Plummer, S., and Schaepman-Strub, G.: An Overview of Global Leaf Area Index
942 (LAI): Methods, Products, Validation, and Applications, 57, 739–799, doi:10.1029/2018RG000608,
943 2019.

944 Garratt, J.: Review: the atmospheric boundary layer, Earth-Science Rev., 37(1–2), 89–134,
945 doi:10.1016/0012-8252(94)90026-4, 1994.

946 Garrigues, S., Lacaze, R., Baret, F., Morisette, J. T., Weiss, M., Nickeson, J. E., Fernandes, R., Plummer,
947 S., Shabanov, N. V., Myneni, R. B., Knyazikhin, Y. and Yang, W.: Validation and intercomparison of
948 global Leaf Area Index products derived from remote sensing data, J Geophys Res Biogeosciences 2005
949 2012, 113(G2), doi:10.1029/2007jg000635, 2008.

950 Gascoin, S., Ducharne, A., Ribstein, P., Perroy, E. and Wagnon, P.: Sensitivity of bare soil albedo to
951 surface soil moisture on the moraine of the Zongo glacier (Bolivia), Geophys. Res. Lett., 36(2), n/a-n/a,
952 doi:10.1029/2008GL036377, 2009.

953 Gill, A. L., Gallinat, A. S., Sanders-DeMott, R., Rigden, A. J., Short Gianotti, D. J., Mantooth, J. A. and
954 Templer, P. H.: Changes in autumn senescence in northern hemisphere deciduous trees: a meta-analysis
955 of autumn phenology studies, Ann. Bot., 116(6), 875–888, doi:10.1093/aob/mcv055, 2015.

956 Grimmond, C. S. B.: The suburban energy balance: Methodological considerations and results for a mid-
957 latitude west coast city under winter and spring conditions, Int. J. Climatol., 12(5), 481–497,
958 doi:10.1002/joc.3370120506, 1992.

959 Grimmond, C. S. B. and Oke, T. R.: An evapotranspiration-interception model for urban areas, Water
960 Resour. Res., 27(7), 1739–1755, doi:10.1029/91WR00557, 1991.

961 Grimmond, C. S. B. and Oke, T. R.: Aerodynamic Properties of Urban Areas Derived from Analysis of
962 Surface Form, J. Appl. Meteorol., 38(9), 1262–1292, doi:10.1175/1520-
963 0450(1999)038<1262:APOUAD>2.0.CO;2, 1999.

964 Grimmond, C. S. B., Oke, T. R. and Steyn, D. G.: Urban Water Balance: 1. A Model for Daily Totals,
965 Water Resour. Res., 22(10), 1397–1403, doi:10.1029/WR022i010p01397, 1986.

966 Grimmond, C. S. B., Cleugh, H. A. and Oke, T. R.: An objective urban heat storage model and its
967 comparison with other schemes, Atmos. Environ. Part B. Urban Atmos., 25(3), 311–326,
968 doi:10.1016/0957-1272(91)90003-W, 1991.

969 Grimmond, C. S. B., King, T. S., Roth, M. and Oke, T. R.: Aerodynamic roughness of urban areas
970 derived from wind observations, Boundary-Layer Meteorol., 89(1), 1–24, doi:10.1023/A:1001525622213,
971 1998.

972 Grimmond, C. S. B., Blackett, M., Best, M. J., Barlow, J., Baik, J. J., Belcher, S. E., Bohnenstengel, S. I.,
973 Calmet, I., Chen, F., Dandou, A., Fortuniak, K., Gouvea, M. L., Hamdi, R., Hendry, M., Kawai, T.,
974 Kawamoto, Y., Kondo, H., Krayenhoff, E. S., Lee, S. H., Loridan, T., Martilli, A., Masson, V., Miao, S.,
975 Oleson, K., Pigeon, G., Porson, A., Ryu, Y. H., Salamanca, F., Shashua-Bar, L., Steeneveld, G. J.,
976 Tombrou, M., Voogt, J., Young, D. and Zhang, N.: The international urban energy balance models
977 comparison project: First results from phase 1, J. Appl. Meteorol. Climatol., 49(6), 1268–1292,
978 doi:10.1175/2010JAMC2354.1, 2010.

979 Harshan, S., Roth, M., Velasco, E. and Demuzere, M.: Evaluation of an urban land surface scheme over a
980 tropical suburban neighborhood, Theor. Appl. Climatol., 133(3–4), 867–886, doi:10.1007/s00704-017-
981 2221-7, 2018.

982 Heiskanen, J., Rautiainen, M., Stenberg, P., Mõttus, M., Vesanto, V.-H., Korhonen, L. and Majasalmi, T.:
983 Seasonal variation in MODIS LAI for a boreal forest area in Finland, Remote Sens Environ, 126, 104–
984 115, doi:10.1016/j.rse.2012.08.001, 2012.

985 Hengl, T., Jesus, J. M. de, MacMillan, R. A., Batjes, N. H., Heuvelink, G. B. M., Ribeiro, E., Samuel-
986 Rosa, A., Kempen, B., Leenaars, J. G. B., Walsh, M. G. and Gonzalez, M. R.: SoilGrids1km — Global
987 Soil Information Based on Automated Mapping, Plos One, 9(8), e105992,
988 doi:10.1371/journal.pone.0105992, 2014.

989 Hengl, T., Jesus, J. M. de, Heuvelink, G. B. M., Gonzalez, M. R., Kilibarda, M., Blagotić, A., Shangguan,
990 W., Wright, M. N., Geng, X., Bauer-Marschallinger, B., Guevara, M. A., Vargas, R., MacMillan, R. A.,
991 Batjes, N. H., Leenaars, J. G. B., Ribeiro, E., Wheeler, I., Mantel, S. and Kempen, B.: SoilGrids250m:
992 Global gridded soil information based on machine learning, Plos One, 12(2), e0169748,
993 doi:10.1371/journal.pone.0169748, 2017.

994 Högström, U.: Non-dimensional wind and temperature profiles in the atmospheric surface layer: A re-
995 evaluation, Boundary-Layer Meteorol., 42(1–2), 55–78, doi:10.1007/BF00119875, 1988.

996 Hoshika, Y., Osada, Y., Marco, A. de, Peñuelas, J. and Paoletti, E.: Global diurnal and nocturnal
997 parameters of stomatal conductance in woody plants and major crops, Global Ecol Biogeogr, 27(2), 257–
998 275, doi:10.1111/geb.12681, 2018.

999 Iwata, H., Hirata, R., Takahashi, Y., Miyabara, Y., Itoh, M. and Iizuka, K.: Partitioning Eddy-Covariance
1000 Methane Fluxes from a Shallow Lake into Diffusive and Ebullitive Fluxes, Boundary-Layer Meteorol.,
1001 169(3), 413–428, doi:10.1007/s10546-018-0383-1, 2018.

1002 Järvi, L., Grimmond, C. S. B. and Christen, A.: The Surface Urban Energy and Water Balance Scheme
1003 (SUEWS): Evaluation in Los Angeles and Vancouver, J. Hydrol., 411(3–4), 219–237,
1004 doi:10.1016/j.jhydrol.2011.10.001, 2011.

1005 Järvi, L., Grimmond, C. S. B., Taka, M., Nordbo, A., Setälä, H. and Strachan, I. B.: Development of the
1006 Surface Urban Energy and Water Balance Scheme (SUEWS) for cold climate cities, Geosci. Model Dev.,
1007 7(4), 1691–1711, doi:10.5194/gmd-7-1691-2014, 2014.

1008 Järvi, L., Havu, M., Ward, H. C., Bellucco, V., McFadden, J. P., Toivonen, T., Heikinheimo, V., Kolari,
1009 P., Riikonen, A. and Grimmond, C. S. B.: Spatial Modeling of Local-Scale Biogenic and Anthropogenic
1010 Carbon Dioxide Emissions in Helsinki, J. Geophys. Res. Atmos., 2018JD029576,
1011 doi:10.1029/2018JD029576, 2019.

1012 Karsisto, P., Fortelius, C., Demuzere, M., Grimmond, C. S. B., Oleson, K. W., Kouznetsov, R., Masson,
1013 V. and Järvi, L.: Seasonal surface urban energy balance and wintertime stability simulated using three
1014 land-surface models in the high-latitude city Helsinki, Q. J. R. Meteorol. Soc., 142(694), 401–417,
1015 doi:10.1002/qj.2659, 2016.

1016 Kawai, T., Ridwan, M. K. and Kanda, M.: Evaluation of the simple urban energy balance model using
1017 selected data from 1-yr flux observations at two cities, J. Appl. Meteorol. Climatol., 48(4), 693–715,
1018 doi:10.1175/2008JAMC1891.1, 2009.

1019 Kent, C. W., Grimmond, S. and Gatey, D.: Aerodynamic roughness parameters in cities: Inclusion of
1020 vegetation, J. Wind Eng. Ind. Aerodyn., 169, 168–176, doi:10.1016/j.jweia.2017.07.016, 2017a.

1021 Kent, C. W., Lee, K., Ward, H. C., Hong, J.-W., Hong, J., Gatey, D. and Grimmond, S.: Aerodynamic
1022 roughness variation with vegetation: analysis in a suburban neighbourhood and a city park, Urban
1023 Ecosyst., doi:10.1007/s11252-017-0710-1, 2017b.

1024 Keyser, T. L., Lentile, L. B., Smith, F. W. and Shepperd, W. D.: Changes in Forest Structure After a
1025 Large, Mixed-Severity Wildfire in Ponderosa Pine Forests of the Black Hills, South Dakota, USA., 2008.

1026 Kokkonen, T. V., Grimmond, C. S. B., Räty, O., Ward, H. C., Christen, A., Oke, T. R., Kotthaus, S. and
1027 Järvi, L.: Sensitivity of Surface Urban Energy and Water Balance Scheme (SUEWS) to downscaling of
1028 reanalysis forcing data, Urban Clim., 23, 36–52, doi:10.1016/j.uclim.2017.05.001, 2018.

1029 Kowalczyk, E. A., Wang, Y. P. and Law, R. M.: The CSIRO Atmosphere Biosphere Land Exchange
1030 (CABLE) model for use in climate models and as an offline model, CSIRO Mar. Atmos. Res. Pap.,
1031 13(November 2015), 1–42, doi:https://doi.org/10.4225/08/58615c6a9a51d, 2006.

1032 Krinner, G., Viovy, N., de Noblet-Ducoudré, N., Ogée, J., Polcher, J., Friedlingstein, P., Ciais, P., Sitch,
1033 S. and Prentice, I. C.: A dynamic global vegetation model for studies of the coupled atmosphere-
1034 biosphere system, Global Biogeochem. Cycles, 19(1), doi:10.1029/2003GB002199, 2005.

1035 Kusaka, H., Kondo, H., Kikegawa, Y. and Kimura, F.: A Simple Single-Layer Urban Canopy Model For
1036 Atmospheric Models: Comparison With Multi-Layer And Slab Models, Boundary-Layer Meteorol.,
1037 101(3), 329–358, doi:10.1023/A:1019207923078, 2001.

1038 Levis, S., Bonan, G. B., Vertenstein, M. and Oleson, K. W.: Technical Documentation and User's Guide
1039 to the Community Land Model's Dynamic Global Vegetation Model, , doi:10.5065/D6P26W36, 2004.

Liu, Y., Xie, R., Hou, P., Li, S., Zhang, H., Ming, B., Long, H. and Liang, S.: Phenological responses of maize to changes in environment when grown at different latitudes in China, F. Crop. Res., 144, 192–199, doi:10.1016/j.fcr.2013.01.003, 2013.

Loridan, T., Grimmond, C. S. B., Offerle, B. D., Young, D. T., Smith, T. E. L., Järvi, L. and Lindberg, F.: Local-Scale Urban Meteorological Parameterization Scheme (LUMPS): Longwave Radiation Parameterization and Seasonality-Related Developments, J. Appl. Meteorol. Climatol., 50(1), 185–202, doi:10.1175/2010JAMC2474.1, 2011.

Margolis, H. A.: AmeriFlux CA-Qcu Quebec - Eastern Boreal, Black Spruce/Jack Pine Cutover, , doi:10.17190/AMF/1246828, 2001.

Martilli, A., Clappier, A. and Rotach, M. W.: An Urban Surface Exchange Parameterisation for Mesoscale Models, Boundary-Layer Meteorol., 104(2), 261–304, doi:10.1023/A:1016099921195, 2002.

Masson, V.: A physically-based scheme for the urban energy budget in atmospheric models, Boundary-Layer Meteorol., 94(3), 357–397, doi:10.1023/A:1002463829265, 2000.

Matsumoto, K., Ohta, T., Nakai, T., Kuwada, T., Daikoku, K., Iida, S., Yabuki, H., Kononov, A. V., Molen, M. K. van der, Kodama, Y., Maximov, T. C., Dolman, A. J. and Hattori, S.: Responses of surface conductance to forest environments in the Far East, Agr Forest Meteorol, 148(12), 1926–1940, doi:10.1016/j.agrformet.2008.09.009, 2008.

McCaughey, J. H.: Energy balance storage terms in a mature mixed forest at Petawawa, Ontario - A case study, Boundary-Layer Meteorol., 31(1), 89–101, doi:10.1007/BF00120036, 1985.

McCuen, R. H.: A Sensitivity and Error Analysis of Procedures Used for Estimating Evaporation, Jawra J Am Water Resour Assoc, 10, 486–497, https://doi.org/10.1111/j.1752-1688.1974.tb00590.x, 1974.

Moene, A. F. and van Dam, J. C.: Transport in the Atmosphere-Vegetation-Soil Continuum, Cambridge University Press., 2013.

Monin, A. S. and Obukhov, A. M.: Basic laws of turbulent mixing in the surface layer of the atmosphere, Contrib. Geophys. Inst. Acad. Sci. USSR, 24(151), 163–187, 1954.

Moureaux, C., Debacq, A., Bodson, B., Heinesch, B., and Aubinet, M.: Annual net ecosystem carbon exchange by a sugar beet crop, Agr Forest Meteorol, 139, 25–39, https://doi.org/10.1016/j.agrformet.2006.05.009, 2006.Monteith, J. L.: Evaporation and environment., Symp. Soc. Exp. Biol., 19(19), 205–34, 1965.

Myneni, R., Knyazikhin, Y. and Park, T.: MCD15A3H MODIS/Terra+Aqua Leaf Area Index/FPAR 4-day L4 Global 500m SIN Grid V006. NASA EOSDIS Land Processes DAAC, 2015.

Nash, J. E. and Sutcliffe, J. V.: River flow forecasting through conceptual models part I — A discussion of principles, J Hydrol, 10, 282–290, https://doi.org/10.1016/0022-1694(70)90255-6, 1970.

Noilhan, J. and Planton, S.: A Simple Parameterization of Land Surface Processes for Meteorological Models, Mon Weather Rev, 117(3), 536–549, doi:10.1175/1520-0493(1989)117<0536:aspols>2.0.co;2, 1989.

United Nations: 2018 revision of world urbanization prospects, 2018.

Nishihama, M., Wolfe, R., Solomon, D., Patt, F., Blanchette, J., Fleig, A. and Masuoka, E.: MODIS Level 1A Earth Location: Algorithm Theoretical Basis Document By the MODIS Science Data Support Team, Greenbelt, Md., 1997.

Noormets, A., McNulty, S. G., DeForest, J. L., Sun, G., Li, Q. and Chen, J.: Drought during canopy development has lasting effect on annual carbon balance in a deciduous temperate forest, New Phytol., 179(3), 818–828, doi:10.1111/j.1469-8137.2008.02501.x, 2008.

Nunez, M., Davies, J. A. and Robinson, P. J.: Surface albedo at a tower site in Lake Ontario, Boundary-Layer Meteorol., 3(1), 77–86, doi:10.1007/BF00769108, 1972.

Offerle, B., Grimmond, C. S. B. and Oke, T. R.: Parameterization of Net All-Wave Radiation for Urban Areas, J. Appl. Meteorol., 42(8), 1157–1173, doi:10.1175/1520-0450(2003)042<1157:PONARF>2.0.CO;2, 2003.

Ogink-Hendriks, M. J.: Modelling surface conductance and transpiration of an oak forest in The Netherlands, Agr Forest Meteorol, 74(1–2), 99–118, doi:10.1016/0168-1923(94)02180-r, 1995.

Oke, T. R.: City size and the urban heat island, Atmospheric Environ 1967, 7(8), 769–779, doi:10.1016/0004-6981(73)90140-6, 1973.

Oke, T. R.: The energetic basis of the urban heat island, Q J Roy Meteor Soc, 108(455), 1 24, doi:10.1002/qj.49710845502, 1982.

OpenStreetMap contributors: OpenStreetMap, *https://www.openstreetmap.org* (Accessed 30 July 2021), 2017

Pastorello, G., Trotta, C., Canfora, E., Chu, H., Christianson, D., Cheah, Y.-W., Poindexter, C., Chen, J., Elbashandy, A., Humphrey, M., Isaac, P., Polidori, D., Reichstein, M., Ribeca, A., Ingen, C. van, Vuichard, N., Zhang, L., Amiro, B., Ammann, C., Arain, M. A., Ardö, J., Arkebauer, T., Arndt, S. K., Arriga, N., Aubinet, M., Aurela, M., Baldocchi, D., Barr, A., Beamesderfer, E., Marchesini, L. B., Bergeron, O., Beringer, J., Bernhofer, C., Berveiller, D., Billesbach, D., Black, T. A., Blanken, P. D., Bohrer, G., Boike, J., Bolstad, P. V., Bonal, D., Bonnefond, J.-M., Bowling, D. R., Bracho, R., Brodeur, J., Brümmer, C., Buchmann, N., Burban, B., Burns, S. P., Buysse, P., Cale, P., Cavagna, M., Cellier, P., Chen, S., Chini, I., Christensen, T. R., Cleverly, J., Collalti, A., Consalvo, C., Cook, B. D., Cook, D., Coursolle, C., Cremonese, E., Curtis, P. S., D'Andrea, E., Rocha, H. da, Dai, X., Davis, K. J., Cinti, B. D., Grandcourt, A. de, Ligne, A. D., Oliveira, R. C. D., Delpierre, N., Desai, A. R., Bella, C. M. D., Tommasi, P. di, Dolman, H., Domingo, F., Dong, G., Dore, S., Duce, P., Dufrêne, E., Dunn, A., Dušek, J., Eamus, D., Eichelmann, U., ElKhidir, H. A. M., Eugster, W., Ewenz, C. M., Ewers, B., Famulari, D., Fares, S., Feigenwinter, I., Feitz, A., Fensholt, R., Filippa, G., Fischer, M., Frank, J., Galvagno, M., et al.: The FLUXNET2015 dataset and the ONEFlux processing pipeline for eddy covariance data, Sci Data, 7(1), 225, doi:10.1038/s41597-020-0534-3, 2020.

Penman, H. L.: Natural evaporation from open water, hare soil and grass, Proc. R. Soc. Lond. A. Math. Phys. Sci., 193(1032), 120–145, doi:10.1098/rspa.1948.0037, 1948.

Peters, E. B., Hiller, R. V. and McFadden, J. P.: Seasonal contributions of vegetation types to suburban evapotranspiration, J. Geophys. Res. Biogeosciences, 116(1), G01003, doi:10.1029/2010JG001463, 2011.

Philip Bloomington, R. and Novick Bloomington, K.: AmeriFlux US-MMS Morgan Monroe State Forest, doi:10.17190/AMF/1246080, 2016.

Porter, C. L.: An Analysis of Variation Between Upland and Lowland Switchgrass, Panicum Virgatum L., in Central Oklahoma, Ecology, 47(6), 980–992, doi:10.2307/1935646, 1966.

Prescher, A.-K., Grünwald, T., and Bernhofer, C.: Land use regulates carbon budgets in eastern Germany: From NEE to NBP, Agr Forest Meteorol, 150, 1016–1025, https://doi.org/10.1016/j.agrformet.2010.03.008, 2010.

Saxton, K. E. and Rawls, W. J.: Soil Water Characteristic Estimates by Texture and Organic Matter for Hydrologic Solutions, Soil Sci. Soc. Am. J., 70, 1569–1578, 2006.

Schmid, H. P., Grimmond, C. S. B., Cropley, F., Offerle, B. and Su, H. B.: Measurements of CO2 and energy fluxes over a mixed hardwood forest in the mid-western United States, Agric. For. Meteorol., 103(4), 357–374, doi:10.1016/S0168-1923(00)00140-4, 2000.

Shuttleworth, W. J.: A simplified one-dimensional theoretical description of the vegetation-atmosphere interaction, Boundary-Layer Meteorol., 14(1), 3–27, doi:10.1007/BF00123986, 1978.

Shuttleworth, W. J.: Evaporation models in the global water budget., Var. Glob. water Budg., 147–171, doi:10.1007/978-94-009-6954-4_11, 1983.

Skamarock, W. C. and Klemp, J. B.: A time-split nonhydrostatic atmospheric model for weather research and forecasting applications, Journal of Computational Physics, 227, 3465–3485, doi:10.1016/j.jcp.2007.01.037, 2008.

Spronken-Smith, R. A., Oke, T. R. and Lowry, W. P.: Advection and the surface energy balance across an irrigated urban park, Int. J. Climatol., 20(9), 1033–1047, doi:10.1002/1097-0088(200007)20:9<1033::AID-JOC508>3.0.CO;2-U, 2000.

Stewart, J. B.: Modelling surface conductance of pine forest, Agr Forest Meteorol, 43(1), 19–35, doi:10.1016/0168-1923(88)90003-2, 1988.

Stoy, P. C., Mauder, M., Foken, T., Marcolla, B., Boegh, E., Ibrom, A., Arain, M. A., Arneth, A., Aurela, M., Bernhofer, C., Cescatti, A., Dellwik, E., Duce, P., Gianelle, D., Gorsel, E. van, Kiely, G., Knohl, A., Margolis, H., McCaughey, H., Merbold, L., Montagnani, L., Papale, D., Reichstein, M., Saunders, M., Serrano-Ortiz, P., Sottocornola, M., Spano, D., Vaccari, F., and Varlagin, A.: A data-driven analysis of energy balance closure across FLUXNET research sites: The role of landscape scale heterogeneity, Agr Forest Meteorol, 171, 137–152, doi:10.1016/j.agrformet.2012.11.004, 2013.

Stöckli, R., Lawrence, D. M., Niu, G. -Y., Oleson, K. W., Thornton, P. E., Yang, Z. -L., Bonan, G. B., Denning, A. S. and Running, S. W.: Use of FLUXNET in the Community Land Model development, J Geophys Res Biogeosciences, 113, G01025, doi:10.1029/2007jg000562, 2008.

Sun, T. and Grimmond, S.: A Python-enhanced urban land surface model SuPy (SUEWS in Python, v2019.2): development, deployment and demonstration, Geosci. Model Dev, 12, 2781–2795, doi:10.5194/gmd-12-2781-2019, 2019.

Sun, T., Järvi, L., Omidvar, H., Theeuwes, N., Lindberg, F., Li, Z. and Grimmond, S.: Urban-Meteorology-Reading/SUEWS: 2020a Release, doi:10.5281/zenodo.3828525, 2020.

Sun, T., Omidvar, H. and Grimmond, S.: Workflow notebooks and FLUXNET2015 data for deriving parameter of SUEWS v2020 based FLUXNET2015 dataset, doi:10.5281/zenodo.5519919, 2021.

van Ulden, A. P. and Holtslag, A. A. M.: Estimation of atmospheric boundary layer parameters for diffusion applications., J. Clim. Appl. Meteorol., 24(11), 1196–1207, doi:10.1175/1520-0450(1985)024<1196:EOABLP>2.0.CO;2, 1985.

Wang, Y., Broxton, P., Fang, Y., Behrangi, A., Barlage, M., Zeng, X., and Niu, G.: A Wet-Bulb Temperature-Based Rain-Snow Partitioning Scheme Improves Snowpack Prediction Over the Drier Western United States, Geophys Res Lett, 46, 13825–13835, doi:10.1029/2019gl085722, 2019.

Ward, H. C., Kotthaus, S., Järvi, L. and Grimmond, C. S. B.: Surface Urban Energy and Water Balance Scheme (SUEWS): Development and evaluation at two UK sites, Urban Clim., 18, 1–32, doi:10.1016/j.uclim.2016.05.001, 2016.

Wolfram Research, NonlinearModelFit, Wolfram Language function, *https://reference.wolfram.com/language/ref/NonlinearModelFit.html* (accessed on 03 Aug 2021). 2008.

Wolfram Research, ClusterClassify, Wolfram Language function, *https://reference.wolfram.com/language/ref/ClusterClassify.html* (accessed on 03 Aug 2021). 2020.

Wright, I. R., Manzi, A. O. and Rocha, H. R. da: Surface conductance of Amazonian pasture: model application and calibration for canopy climate, Agr Forest Meteorol, 75(1–3), 51–70, doi:10.1016/0168-1923(94)02203-v, 1995.